

## Highlights

### **Unveiling the optimization process of Physics Informed Neural Networks: How accurate and competitive can PINNs be?**

Jorge F. Urbán, Petros Stefanou, José A. Pons

- We explore how the optimization process influences convergence and accuracy of Physics-Informed Neural Networks.
- We suggest adjustments to the BFGS optimization algorithm and the mean squared error loss function, which could significantly improve precision by several orders of magnitude.
- We explain our findings by analyzing the conditioning of the Hessian matrix and the spectrum of its eigenvalues.
- We demonstrate that our scheme is applicable to a wide range of physical problems, yielding more accurate results while reducing the computational cost.

# Unveiling the optimization process of Physics Informed Neural Networks: How accurate and competitive can PINNs be?

Jorge F. Urbán<sup>a,\*</sup>, Petros Stefanou<sup>a,b</sup>, José A. Pons<sup>a</sup>

<sup>a</sup>*Departament de Física Aplicada, Universitat d'Alacant, Ap. Correus 99, Alacant, 03830, Comunitat Valenciana, Spain*

<sup>b</sup>*Departament d'Astronomia i Astrofísica, Universitat de València, Dr Moliner 50, València, 46100, Comunitat Valenciana, Spain*

---

## Abstract

This study investigates the potential accuracy boundaries of physics-informed neural networks, contrasting their approach with previous similar works and traditional numerical methods. We find that selecting improved optimization algorithms significantly enhances the accuracy of the results. Simple modifications to the loss function may also improve precision, offering an additional avenue for enhancement. Despite optimization algorithms having a greater impact on convergence than adjustments to the loss function, practical considerations often favor tweaking the latter due to ease of implementation. On a global scale, the integration of an enhanced optimizer and a marginally adjusted loss function enables a reduction in the loss function by several orders of magnitude across diverse physical problems. Consequently, our results obtained using compact networks (typically comprising 2 or 3 layers of 20-30 neurons) achieve accuracies comparable to finite difference schemes employing thousands of grid points. This study encourages the continued advancement of PINNs and associated optimization techniques for broader applications across various fields.

### *Keywords:*

Physics-informed neural networks, optimization algorithms, non-linear PDEs

---

\*Corresponding author

*Email address:* `jorgefrancisco.urban@ua.es` (Jorge F. Urbán)

---

## 1. Introduction

Recent advancements in Physics-Informed Neural Networks (PINNs) have positioned them as serious contenders in the domain of computational physics, disrupting the longstanding monopoly held by classical numerical methods. This disruptive potential arises from their innate ability to integrate domain-specific physics principles with the powerful learning capabilities of neural networks. However, despite their large potential, the nascent nature of this field has left significant gaps in the literature surrounding PINNs. The lack of rigorous mathematical analysis and specificity in methodologies often obscures crucial insights into their limitations, both in terms of accuracy and efficiency.

While PINNs exhibit remarkable adaptability to complex physical systems and have demonstrated interesting results across various domains, their efficacy relies on several factors that warrant closer scrutiny. One critical aspect is the architectural design of the neural network, which influences its ability to capture intricate physical phenomena accurately. Additionally, the choice of loss functions and optimization techniques also play a pivotal role in the overall performance of PINNs. Furthermore, the computational overhead associated with training large-scale PINNs raises questions about their scalability and efficiency, particularly in comparison to established numerical methods that have been optimized over decades.

Addressing these challenges needs a concerted effort from researchers to establish comprehensive benchmarks, standardized evaluation metrics, and theoretical frameworks that elucidate the fundamental principles governing the behavior of PINNs. Only through rigorous analysis and systematic experimentation can we unlock the full potential of PINNs and turn them into reliable tools for solving complex physical problems across diverse fields, ranging from fluid dynamics and solid mechanics to quantum physics and beyond.

Having recognized the need to move beyond the trial-and-error approaches prevalent in most of the PINNs literature, this paper aims to improve our understanding of the fundamental aspects that define their performance. At its core, PINNs training reduces to an optimization problem, prompting us to revisit the basics of optimization theory. We explore some intricacies of PINN optimization, seeking to identify the bottleneck that hinders their precision in

various physical applications. Our focus extends beyond mere adjustments in network size, architecture, activation functions, or other hyperparameters. Instead, we argue that perhaps the most important ingredients are the fundamental principles that govern the optimization process. Through the exploration of different techniques, we bracket the boundaries of precision achievable with PINNs across diverse physical scenarios, focusing on the pivotal role played by the choice of the optimizer in determining the accuracy and efficiency of PINN solutions.

Through our investigation, we demonstrate that seemingly minor modifications in the optimization process can yield substantial enhancements in accuracy, often spanning orders of magnitude. By fine-tuning the optimizer selection, we uncover improvements that result in refined solutions with high precision. Moreover, this allows us to reduce the size of the network in tandem with the choice of optimizer, resulting in significant reductions in computational overhead. This focus-in-optimization approach not only enhances accuracy but also saves computational resources, paving the way for faster and more efficient simulations with PINNs, and enhancing their scalability and applicability across diverse domains of physics and engineering.

The paper is structured as follows: Section 2 provides a brief overview of our PINN framework and discusses key issues related to commonly used optimizers. In Section 3, we thoroughly examine a relatively simple case to demonstrate the significant impact of selecting the appropriate optimizer and how such a choice can minimize network size while achieving excellent results, surpassing previous studies with similar problems. Additionally, in Section 4, we present a comprehensive set of physical problems spanning various fields, illustrating that the insights from the preceding section can be extended to a large variety of problems. Finally, Section 5 summarizes our findings and outlines potential paths for future improvements.

## 2. Summary of the PINNs approach.

Given a set of coordinates  $x_\alpha = (x_1, x_2, x_3, \dots)$  in some domain  $D$ , a general partial differential equation (PDE) that describes the state  $u$  of a physical system can be written in the form

$$\mathcal{L}u(x_\alpha) = G(x_\alpha, u(x_\alpha)), \quad (1)$$

where  $\mathcal{L}$  is a non-linear differential operator and  $G$  is a source term. The PINN approach, as introduced by [1] and [2], solves the problem by finding a

neural network surrogate  $u(x_\alpha; \Theta)$  that approximates the true solution of the problem. The set of parameters  $\Theta$  (i.e. the weights and biases of the neural network) is adjusted iteratively through an optimization process, which tries to minimize a loss function  $\mathcal{J}$  that reflects a global measure of how well is equation (1) satisfied. Typically, the loss function is defined as the mean squared error (MSE) of the residuals for a large number of points  $N$

$$\mathcal{J} = \frac{1}{N} \sum_{i=1}^N \|\mathcal{L}u(x_{\alpha i}; \Theta) - G(x_{\alpha i}, u(x_{\alpha i}; \Theta))\|^2. \quad (2)$$

To completely describe the physical system, we also need to impose boundary conditions on a boundary  $\partial D$ . When Dirichlet and periodic boundary conditions are involved, we impose them through the so-called *hard-enforcement* [1, 3, 4, 5]. This means that we redefine the solution so that they are satisfied by construction independently of the PINN's output. In the case of Dirichlet boundary conditions this can be achieved by redefining the solution in the following way:

$$u(x_\alpha; \Theta) = f_b(x_\alpha) + h_b(x_\alpha)\mathcal{N}(x_\alpha, \Theta), \quad (3)$$

where  $f_b$  is any smooth function that satisfies the Dirichlet boundary conditions when  $x_\alpha \in \partial D$ ,  $h_b$  is a smooth function that is equal to zero when  $x_\alpha \in \partial D$ , and  $\mathcal{N}$  is the output of the PINN.

Periodic boundary conditions can also be readily hard-enforced. For example, let us designate  $x_\beta$  and  $x_\gamma$  as subsets of  $\partial D$  where we apply Dirichlet and periodic boundary conditions, respectively. Then, we redefine the solution as follows:

$$u(x_\alpha; \Theta) = f_b(x_\beta) + h_b(x_\beta)\mathcal{N}(x_\beta, \cos(x_\gamma), \sin(x_\gamma); \Theta). \quad (4)$$

One can indeed check that,  $u$  has the desired behaviour at all the borders: Dirichlet boundary conditions are satisfied because  $u$  is equal to  $f_b$  at the borders of  $x_\beta$  and periodic boundary conditions are satisfied because the coordinates  $x_\gamma$  are first passed to the Fourier basis.

For Neumann or Robin boundary conditions, hard-enforcement is also possible but not straightforward to implement and can result in rather cumbersome and complicated expressions. In these cases, one can always use the soft-enforcement, i.e. add a term in the loss function (2) that takes into

account the residuals of the boundary condition on a sample of points at the boundary.

The loss function  $\mathcal{J}$  is a multidimensional scalar function of the parameters  $\Theta$ . Its minimization requires a robust optimization algorithm that updates the parameters after each training epoch. Two very popular choices in the literature of PINNs are the Adam [6] and BFGS [7, 8, 9, 10] optimizers.

The Adam optimizer has consistently been a fundamental component in the training of various machine learning applications and PINNs. However, it has recently become clear that quasi-Newton methods such as BFGS or its low-memory variant L-BFGS [11] can achieve more accurate results in significantly fewer iterations than Adam, but they are more prone to be trapped at saddle points. The state-of-the-art training schemes involve a combination of these two optimizers, using Adam for the initial iterations to handle better the possible presence of saddle points, and then using BFGS / L-BFGS to accelerate convergence.

### 2.1. Brief review of optimization procedures.

At this point, it is worth reviewing the basic concepts of optimization theory. Both of the aforementioned optimizers can be encompassed in the general family of Line Search methods [12], where the iterative procedure consists of updating the parameters as follows:

$$\Theta_{k+1} = \Theta_k + \alpha_k \mathbf{p}_k, \quad (5)$$

where  $\mathbf{p}_k$  is the direction of the correction step, which depends on the gradient of the loss function and some symmetric matrix  $H_k$

$$\mathbf{p}_k = -H_k \nabla \mathcal{J}(\Theta_k), \quad (6)$$

and  $\alpha_k$  is the step size, which varies depending on the particular method. The parameter  $\alpha_k$  needs to be appropriately chosen to ensure the accuracy of the local gradient estimation and facilitate the loss function reduction, but without impeding convergence by being excessively small.

The simplest case is to consider the gradient decent algorithm, where  $H_k = I$  and  $\alpha_k$  is equal to a small positive constant, which has linear convergence. Adam's method can be recovered by using  $H_k = I$  and a formula for calculating a specific  $\alpha_k$  for each parameter. It can be seen as a more sophisticated variant of the gradient descent algorithm, which has better convergence

properties but is still linear. Newton’s method can be recovered by considering  $H_k$  to be the exact inverse of the Hessian matrix of  $\mathcal{J}$ . It is a second-order method that can converge in very few iterations but with a large increase in the computational cost of each iteration: it requires the explicit calculation of second derivatives of the loss function and the inversion of a high dimensional matrix. The so-called Quasi-Newton methods lie in between. They use some approximation of the inverse Hessian that requires only the first derivatives of the loss function and involves only matrix-vector multiplications, resulting in superlinear convergence (not yet quadratic), but are much faster than Newton’s method per iteration. The step size  $\alpha_k$  is usually chosen with inexact line search procedures that preserve the positive-definiteness of  $H_k$  by imposing certain restrictions on  $\alpha_k$  (for example, the Wolfe conditions [13]).

A general class of quasi-Newton iteration algorithms can be casted under the *self-scaled Broyden* formula. If we define the auxiliary variables

$$\mathbf{s}_k = \Theta_{k+1} - \Theta_k, \quad (7)$$

$$\mathbf{y}_k = \nabla \mathcal{J}(\Theta_{k+1}) - \nabla \mathcal{J}(\Theta_k), \quad (8)$$

$$\mathbf{v}_k = \sqrt{\mathbf{y}_k \cdot H_k \mathbf{y}_k} \left[ \frac{\mathbf{s}_k}{\mathbf{y}_k \cdot \mathbf{s}_k} - \frac{H_k \mathbf{y}_k}{\mathbf{y}_k \cdot H_k \mathbf{y}_k} \right], \quad (9)$$

the next approximation of the inverse Hessian matrix at each iteration can be calculated by (see [14] and [15])

$$H_{k+1} = \frac{1}{\tau_k} \left[ H_k - \frac{H_k \mathbf{y}_k \otimes H_k \mathbf{y}_k}{\mathbf{y}_k \cdot H_k \mathbf{y}_k} + \phi_k \mathbf{v}_k \otimes \mathbf{v}_k \right] + \frac{\mathbf{s}_k \otimes \mathbf{s}_k}{\mathbf{y}_k \cdot \mathbf{s}_k}, \quad (10)$$

where  $\otimes$  denotes the tensor product of two vectors and  $\tau_k, \phi_k$  are respectively the scaling and the updating parameters, which in general change between iterations. For  $\tau_k = 1$  and  $\phi_k = 1$ , we recover the standard BFGS algorithm. Other choices for the value of these parameters define different methods, as we will explore in detail in the next section.

### 3. Case study: neutron star magnetospheres

We now focus on the problem of force-free neutron star magnetospheres in the non-rotating axisymmetric regime as a baseline case. This problem was examined in detail in [16], illustrating the potential of the PINN approach in this particular astrophysical scenario. Here, we revisit this study to highlight

the significant influence that the selection of the optimization algorithm can have on performance. While a detailed exposition of the theoretical background can be found in the aforementioned paper, here we provide a brief overview of the core concepts and equations for completeness.

It is convenient to use compactified spherical coordinates  $x_\alpha = (q, \mu, \phi)$ , where  $q = 1/r$  and  $\mu = \cos \theta$  and introduce dimensionless units  $R$  (radius of the star) and  $B_0$  (surface magnetic field at the equator of the dipolar component). In axisymmetry, the magnetic field  $\mathbf{B}$  can be described in terms of two poloidal and toroidal stream functions  $\mathcal{P}$  and  $\mathcal{T}$  as

$$\mathbf{B} = \frac{q}{\sqrt{1-\mu^2}} (\nabla \mathcal{P} \times \mathbf{e}_\phi + \mathcal{T} \mathbf{e}_\phi). \quad (11)$$

where  $\mathbf{e}_\phi$  is the unit vector in the  $\phi$  direction.

Substituting this expression into the force-free condition  $(\nabla \times \mathbf{B}) \times \mathbf{B} = 0$ , one arrives at the equation

$$\nabla \mathcal{P} \times \nabla \mathcal{T} = 0, \quad (12)$$

which implies that  $\mathcal{T} = \mathcal{T}(\mathcal{P})$ , and the so-called Grad-Shafranov equation

$$\Delta_{\text{GS}} \mathcal{P} + \mathcal{T} \frac{d\mathcal{T}}{d\mathcal{P}} = 0. \quad (13)$$

where we have defined the second order differential operator

$$\begin{aligned} \Delta_{\text{GS}} &= \nabla \cdot \left( \frac{q^2}{1-\mu^2} \nabla \right) \\ &= q^2 \left( q^2 \frac{\partial^2}{\partial q^2} + 2q \frac{\partial}{\partial q} \right) + q^2 (1-\mu^2) \frac{\partial^2}{\partial \mu^2}. \end{aligned} \quad (14)$$

In the general form for the loss function given by equation (2), we can identify  $\mathcal{L} = \Delta_{\text{GS}}$ ,  $G = -\mathcal{T} \frac{d\mathcal{T}}{d\mathcal{P}}$ .

We hard-enforce boundary conditions using equation (3) with

$$f_b(q, \mu) = q (1 - \mu^2) \sum_{l=1}^{l_{\text{max}}} b_l P'_l(\mu) \quad (15)$$

$$h_b(q, \mu) = q(q-1)(1-\mu^2), \quad (16)$$

where  $P_l$  are the Legendre polynomials,  $b_l$  are appropriate coefficients describing the solution at the surface of the star and prime denotes differentiation with respect to  $\mu$ . This reformulation guarantees that  $\mathcal{P}$  equals zero at the axis ( $\mu = \pm 1$ ), vanishes at infinity ( $q = 0$ ), and precisely fulfills the Dirichlet boundary condition at the surface ( $q = 1$ ).



PDE	Layers	Neurons	Iterations (x1000)	Adam it. (x1000)	Batch size (x1000)	Domain
CFGS	1	30	5	2	1	$[0, 1] \times [-1, 1]$
NLGS	2	30	20	10	8	$[0, 1] \times [-1, 1]$

Table 1: Architecture and training hyperparameters for the two cases considered in this section. In both cases, we use a tanh activation function for the hidden layers. The *Neurons* column refers to neurons per hidden layer. The *Adam it.* column refers to the number of iterations where the Adam optimizer is used before switching to a quasi-Newton method. The *Batch size* column refers to the number of points sampling the domain for each training set. The training set changes every 500 iterations in order to sample as many points as possible.

### 3.1. Current-free Grad-Shafranov equation (CFGS)

We begin by considering a current-free magnetosphere with  $\mathcal{T}(\mathcal{P}) = 0$ . Then, equation (13) has an analytical solution given by

$$\mathcal{P}_{\text{an}}(q, \mu) = (1 - \mu^2) \sum_{l=1}^{l_{\text{max}}} q^l b_l P_l'(\mu), \quad (17)$$

which is completely determined by the surface boundary conditions (providing the  $b_l$  coefficients). This is a relatively simple problem to solve but, nevertheless, valuable conclusions can be drawn for the optimization procedure by analyzing it and comparing it with the analytical solution. The complexity of the problem depends on the number of multipoles considered in (17), i.e on the number of non-zero coefficients  $b_l$ . Simpler solutions will achieve the same accuracy with fewer trainable parameters compared to more complex ones. To illustrate this, we focus on a dipole-quadrupole solution ( $b_1, b_2 \neq 0, b_{l>2} = 0$ ). Subsequently, we will extend our findings to encompass a broader range of force-free solutions and various problem types.

#### 3.1.1. Impact of the optimization algorithm

The architecture and training hyperparameters that we use are outlined in table 1. We address the problem utilizing four different optimization updates: Adam, BFGS, self-scaled BFGS (SSBFGS) and self-scaled Broyden (SSBroyden). The first two are usually employed in most PINN applications. The last two methods are variations of equation (10) tailored with specific selections of the parameters  $\tau_k$  and  $\phi_k$ . These methods are well-established

in optimization theory and have demonstrated advantages. In fact, they could be considered as modifications to the BFGS formula rather than new, standalone optimizers. The term "self-scaled" means that  $\tau_k \neq 1$  and corresponds to the usual BFGS formula, but with a scaling factor multiplying the approximation  $H_k$  of the inverse Hessian, while "Broyden" method assumes  $\phi_k \neq 1$ . For SSBFGS we use the choices suggested in [17]:

$$\tau_k^{(1)} = \min \left\{ 1, \frac{\mathbf{y}_k \cdot \mathbf{s}_k}{\mathbf{s}_k \cdot H_k^{-1} \mathbf{s}_k} \right\} \quad (18)$$

$$\phi_k = 1. \quad (19)$$

In [Appendix A](#) we elaborate on the details of this optimizer and show how  $\tau_k^{(1)}$  can be efficiently calculated without the need to invert the matrix  $H_k$ . For SSBroyden we use the choices suggested in [15]:

$$\tau_k^{(2)} = \begin{cases} \tau_k^{(1)} \min \left( \sigma_k^{-1/(n-1)}, \frac{1}{\theta_k^{(1)}} \right) & \text{if } \theta_k > 0 \\ \min \left( \tau_k^{(1)} \sigma_k^{-1/(n-1)}, \sigma_k \right) & \text{if } \theta_k \leq 0, \end{cases} \quad (20)$$

$$\phi_k^{(1)} = \frac{1 - \theta_k}{1 + a_k \theta_k}, \quad (21)$$

where  $n = \text{size}(\Theta_k)$  is the total number of the trainable parameters and  $\sigma_k, \theta_k, a_k$  are intermediate auxiliary variables, whose definitions are given in [Appendix B](#). We should stress here that  $\tau_k$  and  $\phi_k$  should respect certain restrictions in order to ensure global and super-linear convergence of the updating algorithm. Furthermore, the choices presented here are not the only possible ones. We extensively experimented with different options and determined that these choices consistently led to improved convergence and more precise solutions across the diverse range of problems we explored.

Figure 1 shows the evolution of the loss function with the number of iterations for the four optimizers considered. In all cases, we use Adam for the initial training phase in order to avoid possible saddle points and get closer to a global minimum before accelerating convergence with a quasi-Newton method. The impact on the convergence of the quasi-Newton formulae is glaring when compared to Adam. BFGS achieves a loss function that is six orders of magnitude smaller than Adam, which is reduced by a further two and three orders of magnitude by its modifications SSBFGS and SSBroyden respectively. This is further reflected in the absolute and relative errors of  $\mathcal{P}$

and the magnetic field components (which depend on the first derivatives of  $\mathcal{P}$ ), as can be seen in table C.4. For further insight into the error estimates, the interested reader can consult all pertinent details in Appendix C.

The established interpretation for this phenomenon attributes it to a poorly scaled loss function  $\mathcal{J}$ , which results in an ill-conditioned Hessian matrix  $\text{hess}(\mathcal{J})$  close to the minimum [18, 19, 20]. This characteristic is intrinsic to PINN configurations and is associated with formulating the loss function based on a differential operator [21, 22].

An approach to grasp this phenomenon is through an examination of the spectrum of the Hessian matrix. As depicted in Figure 2,  $\text{hess}(\mathcal{J})$  demonstrates a broad eigenvalue spectrum, with numerous eigenvalues closely approaching zero and some outliers displaying larger magnitudes. Additionally, the condition number, represented by

$$\kappa = \frac{\lambda_{max}}{\lambda_{min}}, \quad (22)$$

where  $\lambda_{max}$  and  $\lambda_{min}$  denote the eigenvalues of the largest and smallest magnitude respectively, is notably large (on the order of  $\kappa \sim 10^{12}$ ). These characteristics confirm the ill-conditioning of  $\text{hess}(\mathcal{J})$ , indicating that certain directions within the trainable parameter space  $\Theta$  lead to significantly larger changes in the loss function compared to others. In the conventional analogy of “descending a mountain”, this scenario aligns with encountering long, extended valleys where certain directions exhibit steep gradients while others remain relatively flat.

Gradient descent techniques like Adam proceed by advancing along the steepest direction, leading to a perpetual zig-zagging along the valley and making minimal progress towards the minimum. Quasi-Newton methods outperform Adam by incorporating knowledge of the local curvature of  $\mathcal{J}$  via the Hessian, thus identifying superior descent directions. However, findings from computational experiments in [23] and [24] reveal that the efficacy of the standard BFGS algorithm might still suffer due to ill-conditioning. They argue that it could be challenging for line search methods to determine a suitable step size  $\alpha_k$ , and suggest the use of self-scaled methods as a countermeasure.

Another way of understanding the influence of quasi-Newton methods, as pointed out in [21, 22], is through the preconditioning of the loss function. At every iteration step, the inverse Hessian approximation acts as a

preconditioner that maps the parameter space  $\Theta$ , where the Hessian is ill-conditioned, to a new space  $\mathbf{z} = H_k^{-1/2}\Theta$ , where the conditioning is much better. The rate of convergence of the different quasi-Newton methods will be strongly affected by the conditioning of the Hessian in this new space. To observe this effect mathematically, consider that representing equation (5) in the  $\mathbf{z}$  space, corresponds to the usual formula of a gradient-descent method

$$\mathbf{z}_{k+1} = \mathbf{z}_k - \alpha_k \nabla \mathcal{J}(\mathbf{z}_k). \quad (23)$$

However, the landscape of the loss function in this space is considerably more uniform (without long valleys) compared to the  $\Theta$  space. A step along the direction of the gradient genuinely advances towards the minimum. Meanwhile, as we approach the minimum, the Hessian of the new space  $\mathbf{z}$

$$\text{hess}(\mathcal{J}(\mathbf{z})) = H_k^{1/2} \text{hess}(\mathcal{J}(\Theta)) H_k^{1/2}, \quad (24)$$

might also start to be ill-conditioned and the rate of convergence would, eventually, deteriorate. This depends crucially on the updating formula of  $H_k$ , which explains the improved performance of the modifications of the standard BFGS formula that we investigate here.

Please note that while the exact Newton’s formula theoretically promises perfect conditioning, ensuring uniform gradients in all directions, its practical implementation poses numerical challenges. This is due to the necessity of solving an ill-conditioned linear system of equations to determine the Newton descent direction. Typically, such ill-conditioning arises from slight variations in matrix coefficients, particularly in the Hessian, resulting in significant deviations in the solution accuracy ([25]).

To appreciate the effect of the Hessian conditioning, figure 3 shows the spectra of the Hessian expressed in the  $\mathbf{z}$  space for each optimization algorithm. Each of these histograms is computed by letting the PINN to be trained additional iterations with a fixed training set until we arrive to similar values of  $\mathcal{J}$ , which we set to be very low ( $\mathcal{J} \sim 10^{-13}$ ) in order to be close to the minimum. As we can observe, the standard BFGS algorithm gives an ill-conditioned Hessian in the  $\mathbf{z}$  space close to the minimum, whereas with the BFGS modifications we obtain better-conditioned matrices. This is reflected in the number of iterations needed for each algorithm to arrive at the value of loss prescribed above: the BFGS algorithm needed  $\sim 40000$  iterations, whereas the BFGS modifications only needed  $\sim 1000$ .

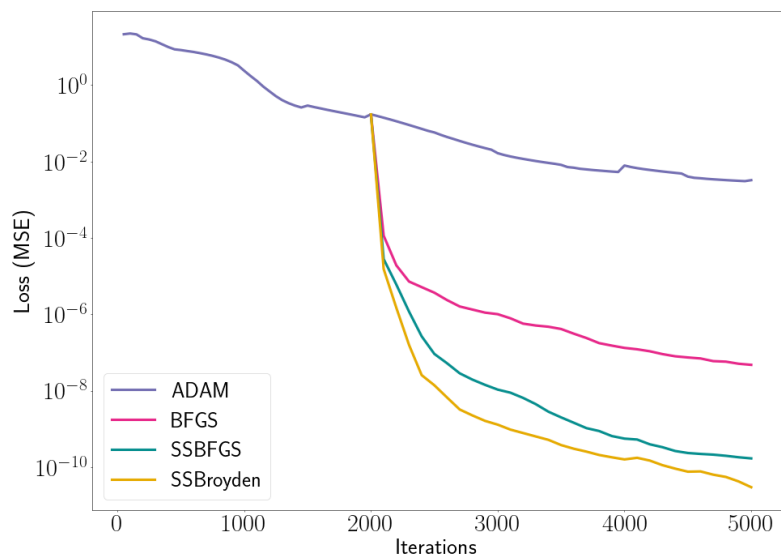


Figure 1: Loss function vs. iterations for the current-free Grad-Shafranov equation. Results are obtained for the four optimization algorithms considered in section 3.1.1.

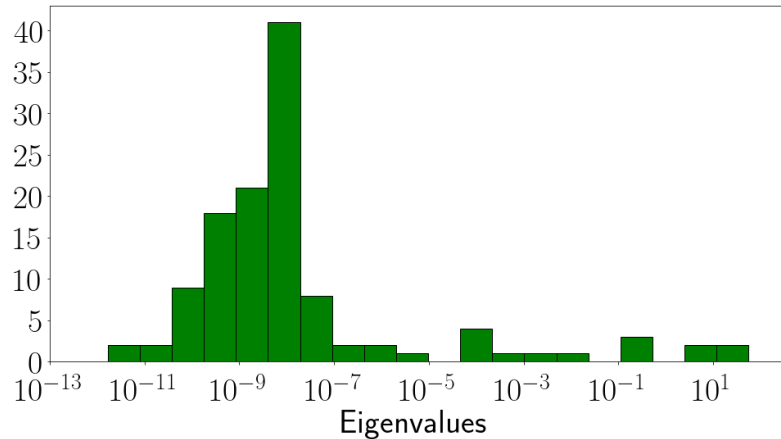
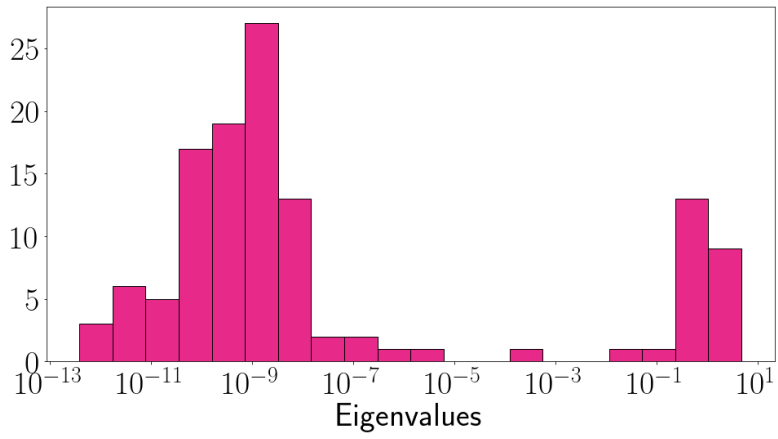
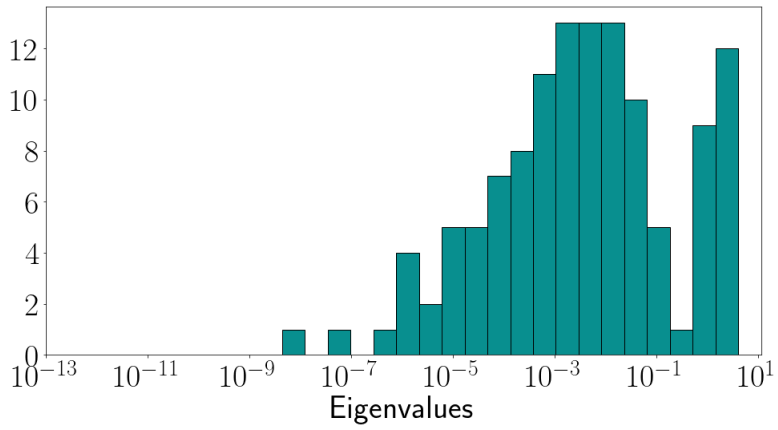


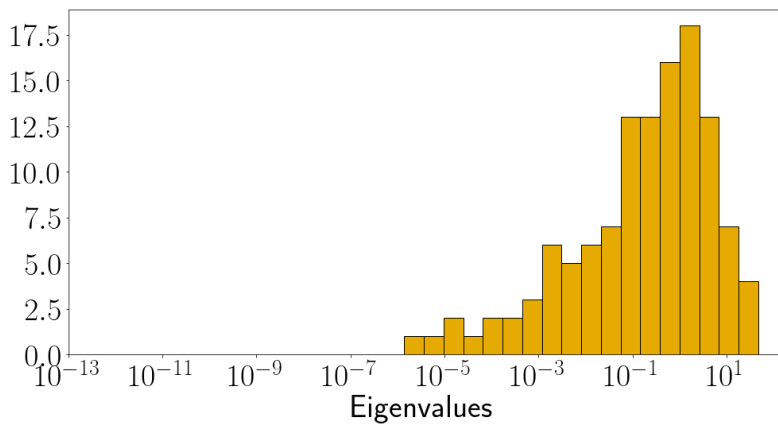
Figure 2: Eigenvalue spectrum of  $\text{hess}(\mathcal{J}(\Theta))$ . It is obtained after the loss function has been reduced to  $\mathcal{J} \sim 10^{-13}$  for a fixed set of points in order to be as close to the minimum as possible.



(a)



(b)



(c)

Figure 3: Eigenvalue spectra of the preconditioned Hessian matrix  $\text{hess}(\mathcal{J}z)$  for BFGS (3a), SSBFGS (3b) and SSBroyden (3c).

### 3.1.2. Impact of the loss function.

In a similar light, we can investigate the effect of using a slightly modified version of the usual MSE loss function (2). In particular, we explore the consequences of a general approach, evaluating the loss function through a user-defined monotonically increasing function  $g$ :

$$\mathcal{J}_g = g(\mathcal{J}). \quad (25)$$

The Hessian matrices  $\text{hess}(\mathcal{J})$  and  $\text{hess}(\mathcal{J}_g)$ , associated respectively with the functions  $\mathcal{J}$  and  $\mathcal{J}_g$ , are related by

$$\text{hess}(\mathcal{J}_g) = g'(\mathcal{J})\text{hess}(\mathcal{J}) + g''(\mathcal{J})\nabla\mathcal{J} \otimes \nabla\mathcal{J}. \quad (26)$$

Near the minimum, the second term in brackets can be neglected, because  $\nabla\mathcal{J} \simeq 0$ , and both Hessian matrices are proportionally related to each other with ratio  $g'(\mathcal{J})$ . Two obvious choices for  $\mathcal{J}_g$  are

$$\mathcal{J}_{1/2} \equiv \sqrt{\mathcal{J}}, \quad (27)$$

$$\mathcal{J}_{\log} \equiv \log \mathcal{J}. \quad (28)$$

Since both the square root and the natural logarithm exhibit derivatives exceeding 1 when  $\mathcal{J} \ll 1$ , they have the potential to accelerate convergence. We demonstrate this by training three identical networks with different loss functions, namely  $\mathcal{J}, \mathcal{J}_{1/2}, \mathcal{J}_{\log}$ . We use the standard BFGS algorithm in order to isolate the impact of the loss function modifications from that of the BFGS modifications.

When  $\mathcal{J} > 1$  the loss function modifications could have the opposite effect, i.e. decelerate convergence because of the decreased slope of  $\mathcal{J}_g$ . To prevent this, we utilize  $\mathcal{J}_g$  exclusively during the BFGS phase of training, while maintaining the use of  $\mathcal{J}$  during the Adam stage. Figure 4 illustrates the effect of the loss function modifications on convergence. Please observe that, for comparison purposes, we represent the standard MSE loss  $\mathcal{J}$  in the plot, while the actual training has been conducted using the corresponding  $\mathcal{J}_g$ . We achieve an improvement of roughly two orders of magnitude by evaluating the loss through a monotonic function  $g$ , everything else being equal.  $\mathcal{J}_{\log}$  converges slightly faster than  $\mathcal{J}_{1/2}$  because its slope is steeper close to the minimum. This enhancement becomes more evident when examining the relative error norms of the PDE solution  $\mathcal{P}$  and its derivatives, as presented in table C.5.

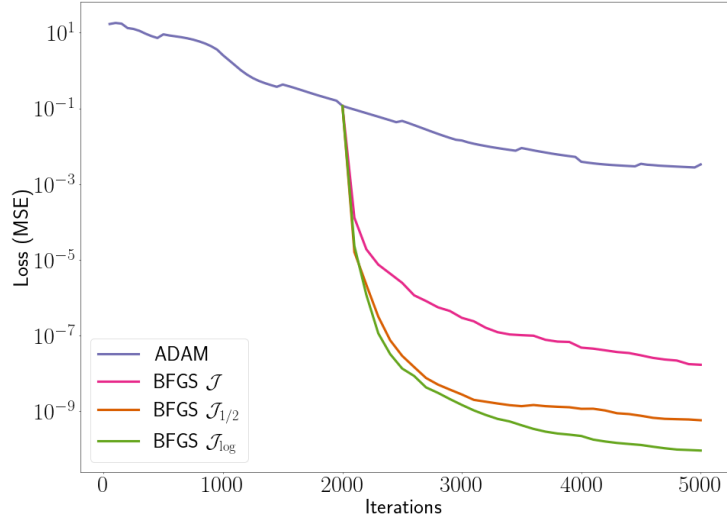
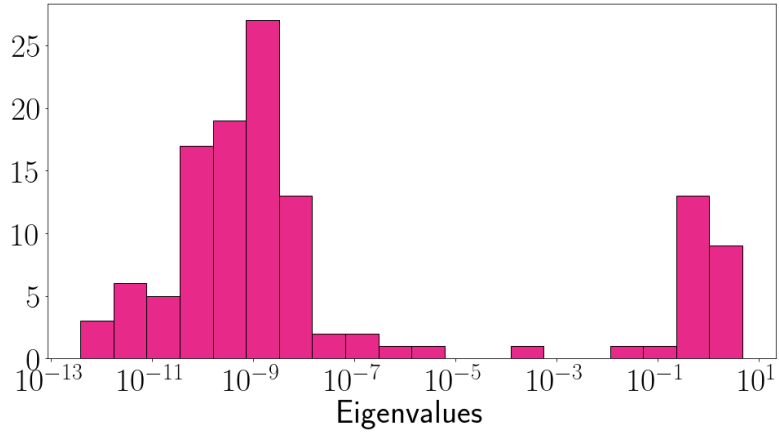


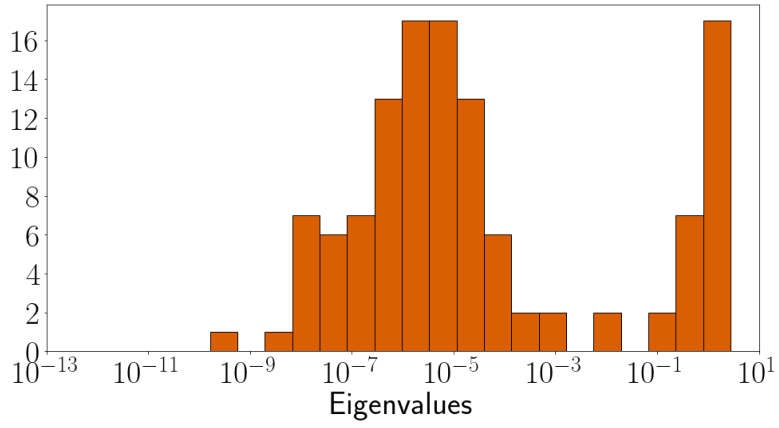
Figure 4: Loss function vs. iterations for the current-free Grad-Shafranov equation. Results are obtained for the loss function modifications considered in section 3.1.2. Note that we plot the MSE loss (2) and not the modifications (25) used during training. In all cases, the standard BFGS algorithm is used.

As in the previous section, one can attribute the improved convergence to the better conditioning of the Hessian matrix. We employ the same optimization algorithm in all cases. However, since we minimize different loss functions, the inverse Hessian approximations vary at each iteration. Consequently, the preconditioned Hessian  $\text{hess}(\mathcal{J}_g(\mathbf{z}))$  may exhibit different condition numbers  $\kappa$  depending on the selection of  $g$ . Indeed, by analyzing the eigenvalue spectra of figure 5, it is apparent that  $\mathcal{J}_{\log}$  exhibits a smaller condition number compared to  $\mathcal{J}$ , with more eigenvalues clustered around unity and the majority of its eigenvalues concentrated at higher values. All these features suggest a better-conditioned Hessian matrix and explain its superior performance. Similar observations hold for  $\mathcal{J}_{1/2}$ .

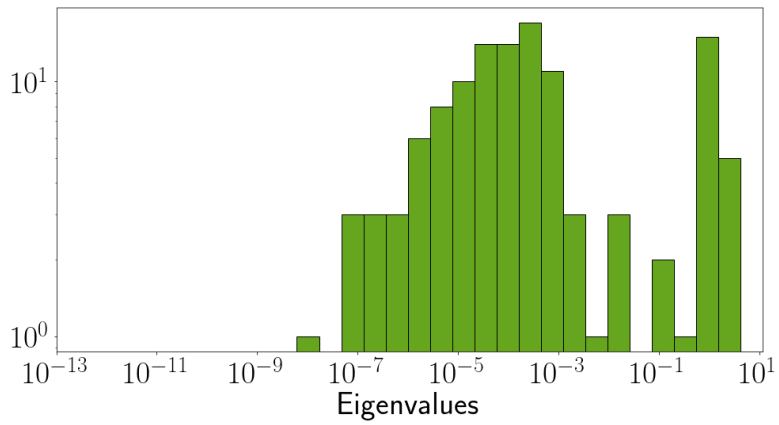




(a)



(b)



(c)

Figure 5: Eigenvalue spectra of the preconditioned Hessian matrix  $\text{hess}(\mathcal{J}(z))$  for  $\mathcal{J}$  (5a),  $\mathcal{J}_{1/2}$  (5b), and  $\mathcal{J}_{\log}$  (5c).

Changes to the loss function can be implemented combined with the selection of a better optimization algorithm. For the range of choices that we have explored, the latter seem to have a more pronounced effect on convergence. Using a combination of the best choices in each case can lead to overall better results, as seen in figure 6. In practice, however, it is much simpler to change the loss function than to modify an existing optimizer or to develop a new one.

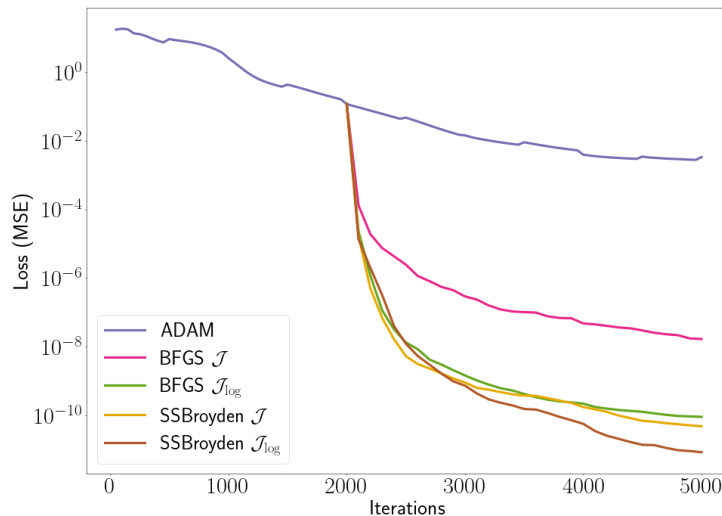


Figure 6: Loss function vs. iterations for the current-free Grad-Shafranov equation considering various combinations of optimization algorithm/loss function modifications.

### 3.2. Non-linear force-free solutions with higher order multipoles (NLGS)

Up to now, our emphasis has been on a relatively simple, linear problem as to illustrate how enhancements in the optimization process can significantly improve the solution accuracy. Moving forward, we now show that our results generalize nicely to more complex solutions of the Grad-Shafranov equation.

We consider a non-linear force-free magnetospheric model by introducing a toroidal function similar to the one chosen in [26] but generalized for negative values of  $\mathcal{P}$ . This is:

$$\mathcal{T}(\mathcal{P}) = \begin{cases} s(|\mathcal{P}| - \mathcal{P}_c)^\sigma & \text{if } |\mathcal{P}| > \mathcal{P}_c \\ 0 & \text{if } |\mathcal{P}| < \mathcal{P}_c, \end{cases} \quad (29)$$

where  $(s, \mathcal{P}_c, \sigma)$  are parameters that control the relative strength of the toroidal and the poloidal magnetic fields, the extent of the current-filled

region, and the degree of non-linearity of the model, respectively. At the surface of the star, the boundary condition consists of eight multipoles, so that  $b_{l \leq 8} \neq 0$  in equation (15).

The presence of non-linearity and a highly multipolar structure significantly increase the solution’s complexity. Consequently, larger networks with a larger number of trainable parameters are necessary to attain comparable precision. Nevertheless, because of the efficient optimization, we manage to keep the network size rather small even for this problem. Table 1 contains the training and architecture hyperparameters.

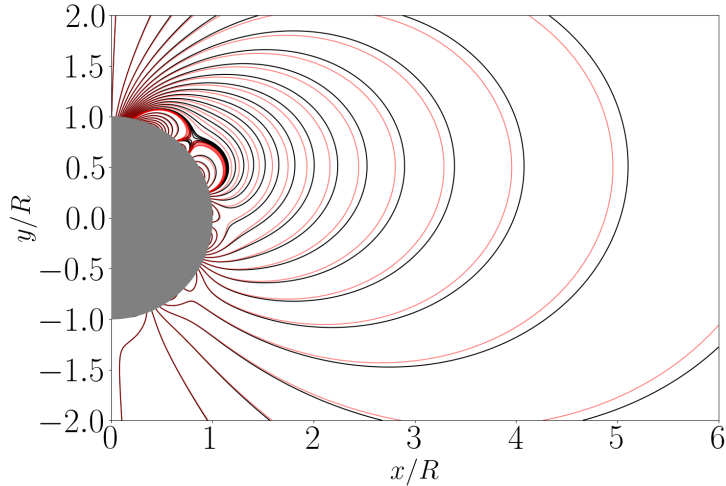


Figure 7: Magnetic field lines obtained for the force-free case (black). The field lines corresponding to the current-free case are also plotted for comparison.

Analytical solutions are not available for the non-linear Grad-Shafranov equation, thus making it impossible to calculate the error of our solution through direct comparison. Instead, we adopt the approach that we introduced in [16]: we create a regular grid  $\{q_i, \mu_j\}_{i,j=1}^{N_0}$ , and we evaluate the PINN solution  $\mathcal{P}$  at all points in the grid using a forward pass. Then, we discretize the PDE (13) using a second-order finite differences scheme. If  $\mathcal{P}$  was the exact solution of the PDE, the  $L_2$ -error of the discretized PDE  $\epsilon_{\text{FD}}$  would decrease with increasing resolution as  $\sim N_0^{-2}$ . In reality,  $\mathcal{P}$  is only an approximate solution with an intrinsic error  $\epsilon_{\text{NN}}$  inherited from the quality and accuracy of the PINN. Therefore,  $\epsilon_{\text{FD}}$  will follow this power law only up to the point where the PINN approximation error  $\epsilon_{\text{NN}}$  starts to be important compared to the discretization error  $\epsilon_{\text{FD}}$  and, as a consequence, it will stag-

nate to the value of  $\epsilon_{\text{NN}}$ . If the PINN approximation is not accurate, this will happen at a relatively low resolution. On the other hand, if  $\epsilon_{\text{FD}}$  dominates  $\epsilon_{\text{NN}}$  for high resolutions, then the PINN should be very close to the exact solution.

Figure 8 shows the performance of the BFGS modifications (top panels) and of the loss function modifications (bottom panels) on this problem. The left panels depict the evolution of the loss function with the number of iterations, whereas the right panels illustrate the estimation of the real errors, as outlined previously ( $L_2$ -error of the discretized PDE as a function of the number of grid points  $N_0$ ). We see that the improvement in convergence and precision is massive for this complicated problem just as for the simple problem of section 3.1.

The PINN error when the standard BFGS algorithm is used for training is about  $\epsilon_{\text{NN}} \sim 10^{-3}$ . SSBFGS and SSBroyden achieve much lower errors. Specifically,  $\epsilon_{\text{NN}}$  begins to surpass  $\epsilon_{\text{FD}}$  at an approximate resolution of  $4500 \times 4500$  (not depicted in the figure), near the memory limit of the machine employed for generating the results in this paper. Note that, since our discretization scheme is second order, the absolute error of the PDE is  $\epsilon_{\text{NN}}^2$ . In table C.6 we gather detailed error metrics for all the BFGS algorithm / loss function modifications we have used. In brief, aiming for a comparable precision level ( $< 10^{-4}$ ) with a second-order finite difference scheme would require a grid comprising at least  $1000 \times 1000$  points for this 2D problem. In higher dimensions, the advantages of PINNs would become even more pronounced.

### 3.3. Parameter study

The impact of the modifications introduced before may depend on the size of the network. Hence, we now focus on a hyperparameter study, where we explore how the accuracy of the PINN approximation varies with the number of neurons per layer or the number of layers. For each model, we keep fixed all choices regarding the number of training points, the number of iterations, etc. Figure 9 shows the values of  $\epsilon_{\text{NN}}$  as a function of the neurons in each layer, obtained for the SSBroyden algorithm with  $\mathcal{J}$  and for the BFGS algorithm with  $\mathcal{J}_{\log}$  for different depths (that is, varying the number of hidden layers). The results obtained with BFGS and  $\mathcal{J}$  are also plotted for comparison purposes.

For simpler networks consisting of just one layer, these adjustments have a relatively minor effect. However, for networks with 2-3 layers, there is a

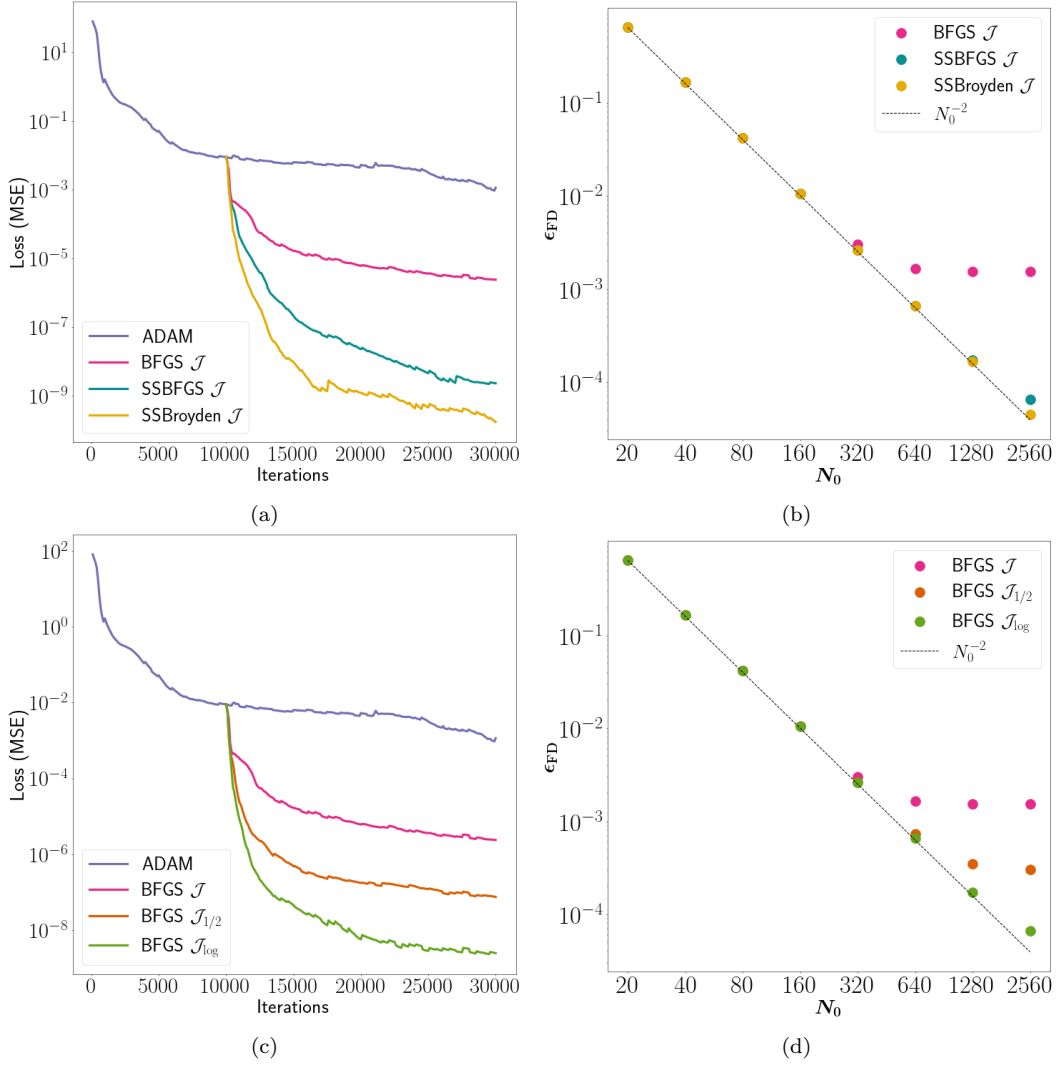


Figure 8: Left: Loss function vs. iterations for the non-linear Grad-Shafranov equation. Results are obtained considering the BFGS algorithm modifications with the standard loss function (upper) and for the loss function modifications with the standard BFGS algorithm (lower). Right:  $L_2$  norm of the discretized PDE as a function of the grid resolution  $N_0$  obtained for each case.

significant boost in accuracy when a certain minimum number of neurons is employed. While simply increasing the number of parameters leads to a gradual reduction in error, our proposed enhancements lead to a much faster decline. This underscores the significance of refining the optimization process

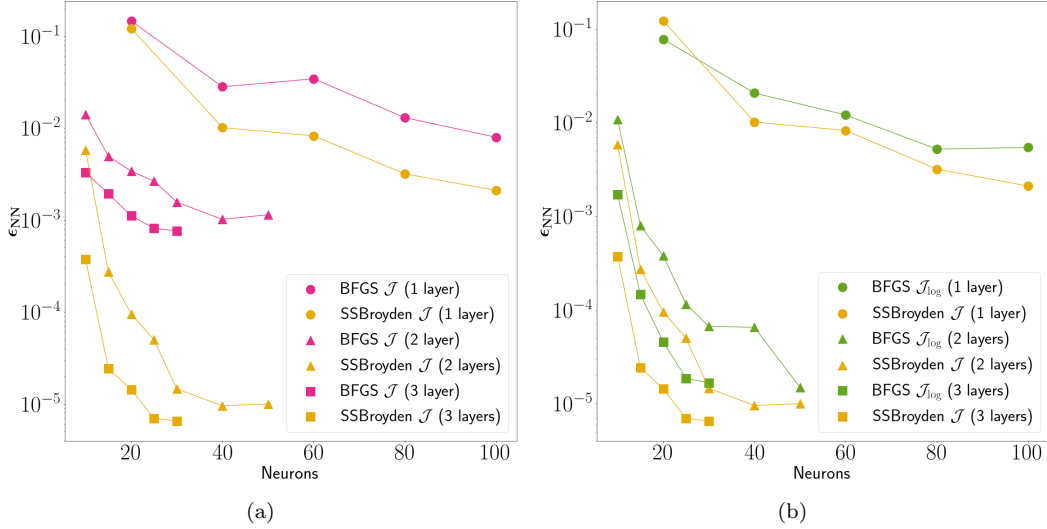


Figure 9: Approximation error  $\epsilon_{NN}$  for different depths as a function of the neurons in every layer. Left panel (9a): comparison between using BFGS and  $\mathcal{J}$  and SSBroyden with  $\mathcal{J}$ . Right panel (9b): comparison between using BFGS with  $\mathcal{J}_{log}$  and SSBroyden with  $\mathcal{J}$ .

over indiscriminately enlarging the network size. The right panel of figure 9 demonstrates that the impact of the optimizer outweighs slightly the effect of redefining the loss function. However, it is worth noting that the latter adjustment involves simply changing a single line of code.

In summary, using networks comprising 2 or 3 hidden layers with around 30 – 40 neurons each, we achieve highly precise results for this specific problem. In the following section, we will show that networks of similar dimensions suffice to yield results of similar accuracy across various physical applications governed by different equations.

#### 4. Other physics problems

Our analysis of the optimization process and how it can benefit from modifications of the optimizer or the loss function is not problem specific and is not tailored to neutron star magnetospheres. To showcase its broad effectiveness, we now discuss solutions for diverse PDEs across various fields and applications. In this section, we cover cases with higher order derivatives, more dimensions, various degrees of non-linearity, time-dependence, systems of equations etc.

PDE	Layers	Neurons	Iterations (x1000)	Adam it. (x1000)	Batch size (x1000)	Domain
NLP	2	30	20	10	8	$[0, 1] \times [-1, 1]$
NLS	2	40	20	10	10	$[0, \pi/2] \times [-15, 15]$
KdV	3	30	20	10	10	$[0, 5] \times [0, 20]$
3DNS	2	40	20	10	10	$[0, 1] \times [-1, 1]^3$

Table 2: Same as Table 2 for the physical applications in this section.

For each case, we provide a concise description of each PDE along with the context in which it is applied. Then we specify how we formulate each problem in accordance with the notation of section 2. The architecture and training hyperparameters can be found in table 2.

In figure 11 we show the evolution of the loss function with the number of iterations for all problems, reaffirming that the findings outlined in section 3 hold universally. In all cases, we use the Adam optimizer and the standard MSE loss  $\mathcal{J}$  for the initial training phase (10000 iterations). After that, we train using either BFGS with  $\mathcal{J}_{\log}$  or using SSBroyden with  $\mathcal{J}$ , which were the most competitive combinations of modifications in section 3. In Appendix C, we provide additional tables detailing the errors and precision attained in each scenario.

***Non-linear Poisson equation (NLP).*** We solve the Poisson equation with a non-linear (exponential) term, as considered in [27]

$$\nabla^2 \phi - e^\phi = r(x, y). \quad (30)$$

If  $r(x, y) = 0$ , it is also called the Liouville equation in the context of differential geometry. It has application in various fields, such as hydrodynamics, to describe mean field vorticity in steady flows [28, 29] and Quantum Field Theory, in the Chern-Simons theory [30, 31].

To construct the loss function (2), we can identify  $\mathcal{L} = \nabla^2$  and  $G = e^\phi + r(x, y)$ . The function  $r(x, y)$  is chosen such that the function

$$\phi(x, y) = 1 + \sin(k\pi x) \cos(k\pi y), \quad (31)$$

is a solution of the PDE, for some  $k \in \mathbb{Z}$ . We solve the problem in Cartesian

coordinates  $x_\alpha = (x, y)$  with Dirichlet boundary conditions

$$\phi(0, y) = \phi(1, y) = 1, \quad (32)$$

$$\phi(x, 0) = 1 + \sin(k\pi x), \quad (33)$$

$$\phi(x, 1) = 1 + \sin(k\pi x) \cos(k\pi), \quad (34)$$

which can be hard-enforced through the following definitions

$$f_b(x, y) = 1 + [1 - y(1 - \cos(k\pi))] \sin(k\pi x), \quad (35)$$

$$h_b(x, y) = xy(1-x)(1-y). \quad (36)$$

In [27] they consider the simplest case with  $k = 1$ . We decided to raise this number to  $k = 4$ , in order to get a more pronounced oscillatory behavior, that would challenge our solver. Results for the loss function and the error estimations can be found in figure 11a and in table C.7.

**Non-linear Schrödinger equation (NLS).** We solve the time-dependent Schrödinger equation in 1D, written in convenient units to avoid  $\hbar$  prefactors as

$$i \frac{\partial \Psi}{\partial t} = -\frac{1}{2} \frac{\partial^2 \Psi}{\partial x^2} + V \Psi, \quad (37)$$

where  $i$  is the imaginary unit, and  $V(\Psi) = -|\Psi|^2$  is a non-linear potential.  $\Psi$  is, in general, a function whose image lies in  $\mathbb{C}$ . Hence, if we denote  $\Psi(x, t) \equiv u(x, t) + iv(x, t)$ , we obtain the following non-linear coupled system of PDEs

$$\frac{\partial v}{\partial t} - \frac{\partial^2 u}{\partial x^2} - (u^2 + v^2) u = 0, \quad (38)$$

$$\frac{\partial u}{\partial t} + \frac{\partial^2 v}{\partial x^2} + (u^2 + v^2) v = 0. \quad (39)$$

The non-linear Schrödinger equation describes the dynamics of a non-linear wave packet in dispersive media. In the context of Bose-Einstein condensate, it is known as the Gross-Pitaevskii equation [32, 33]. This equation is widely applicable in different physical scenarios, such as fluid mechanics, in order to model small-amplitude gravity waves [34], superconductivity and superfluidity [35, 36, 37], or non-linear optics [38], among others.

The loss function is defined as the sum of two terms, which we construct according to equation (2) by identifying  $\mathcal{L}_v = \frac{\partial}{\partial t} - uv$ ,  $G_v = \frac{\partial^2 u}{\partial x^2} + u^3$  and  $\mathcal{L}_u = \frac{\partial}{\partial t} + uv$ ,  $G_u = -\frac{\partial^2 v}{\partial x^2} - v^3$ .



We enforce periodic boundary conditions in the x-direction and adopt identical initial conditions as those examined in [2], namely  $(u_0(x), v_0(x)) = (2\text{sech}(x), 0)$ . Note that neither  $u_0$  nor its derivatives are periodic, but they decay to zero for large  $|x|$ . We extend the boundaries to  $x = \pm 15$  instead of  $x = \pm 5$  that was used in [2] to ensure sufficient decay, but we keep the same limits for the time domain. Boundary/initial conditions for  $u$  and  $v$  are introduced via hard-enforcement using equation (4):

$$u(t, x) = u_0(x) + t\mathcal{N}_u \left[ t, \cos\left(\frac{2\pi x}{L}\right), \sin\left(\frac{2\pi x}{L}\right) \right], \quad (40)$$

$$v(t, x) = v_0(x) + t\mathcal{N}_v \left[ t, \cos\left(\frac{2\pi x}{L}\right), \sin\left(\frac{2\pi x}{L}\right) \right], \quad (41)$$

Results for the loss function and the error estimations can be found in figure 11b and in table C.8

**Korteweg-De Vries equation (KdV).** We solve the Korteweg-De Vries (KdV) equation

$$\alpha \frac{\partial u}{\partial t} + \beta u \frac{\partial u}{\partial x} + \gamma \frac{\partial^3 u}{\partial x^3} = 0, \quad (42)$$

where  $\alpha$ ,  $\beta$  and  $\gamma$  are constants, whose standard values in the literature are  $\alpha = 1$ ,  $\beta = 6$ ,  $\gamma = 1$ .

This equation characterizes the dynamics of non-linear dispersive waves, observed in shallow waters or plasma [39]. It encapsulates the fundamental principles governing these wave phenomena and has found extensive application not only in fluid mechanics but also in plasma physics [40] and non-linear optics [41]. It serves as a robust test because of the presence of an important non-linear term (Burgers-like) and a third order derivative. In this example, we reproduce a relatively difficult solution: the two-soliton solution, which can be written as

$$u_{\text{an}}(x, t) = \frac{2(c_1 - c_2) \left[ c_1 \text{ch}^2\left(\sqrt{c_2} \frac{\zeta_2}{2}\right) + c_2 \text{sh}^2\left(\sqrt{c_1} \frac{\zeta_1}{2}\right) \right]}{\left[ (\sqrt{c_1} - \sqrt{c_2}) \text{ch}\left(\frac{\sqrt{c_1}\zeta_1 + \sqrt{c_2}\zeta_2}{2}\right) + (\sqrt{c_1} + \sqrt{c_2}) \text{ch}\left(\frac{\sqrt{c_1}\zeta_1 - \sqrt{c_2}\zeta_2}{2}\right) \right]^2}. \quad (43)$$

Here we denote the hyperbolic sine and cosine as sh and ch respectively and we define  $\zeta_i \equiv x - c_i t - x_i$ , being  $c_i$  and  $x_i$  arbitrary constants which describe the speed and the initial position of the solitons. Initial and boundary

conditions are given following [42]

$$u(0, x) = u_0(x), \quad (44)$$

$$u(t, x_0) = g_1(t), \quad (45)$$

$$u(t, x_0 + L) = g_2(t), \quad (46)$$

$$\partial_x u(t, x_0 + L) = g_3(t), \quad (47)$$

where  $L$  is the size of the spacial domain and  $u_0(x), g_1(t), g_2(t), g_3(t)$  are suitable functions selected to produce the analytical solution (43). We construct the loss function using  $\mathcal{L} = \frac{\partial}{\partial t} + 6u\frac{\partial}{\partial x} + \frac{\partial^3}{\partial x^3}$  and  $G = 0$  in equation (2). We hard-enforce the Dirichlet boundary conditions by prescribing

$$f_b(t, x) = u_0(x) + A(t, x), \quad (48)$$

$$A(t, x) = \frac{1}{L} [(x - x_0)(g_2(t) - g_2(0)) + (x_0 + L - x)(g_1(t) - g_1(0))], \quad (49)$$

$$h_b(t, x) = t(x - x_0)(x - x_0 - L). \quad (50)$$

The Neumann condition (47) is imposed via soft-enforcement as an additional term in the loss function. The total loss function is therefore calculated as  $\mathcal{J} = \mathcal{J}_{\text{PDE}} + \frac{\lambda}{N_b} \sum_{i=1}^{N_b} \|\frac{\partial}{\partial x} u(t, x_0 + L) - g_3(t)\|^2$ , where  $N_b$  is the number of points considered at the boundary and  $\lambda$  is a hyperparameter to balance both terms. We set  $N_b = 1000$  and  $\lambda = 5$ , as we found accurate results with these particular choices.

We choose an initial condition such that the two solitons have initial positions  $x_1 = -2, x_2 = 2$  and initial velocities  $c_1 = 6, c_2 = 2$ . Since  $x_1 < x_2$  but  $c_1 > c_2$ , eventually, the solitons will collide, triggering a non-linear interaction between them. We selected the aforementioned values to ensure that this interaction is significant and observable within the time domain under consideration. Before or after this interaction, the solitons will travel as a linear superposition of waves (that is, as single solitons) with their respective velocities. Fig. 10 shows four snapshots of the solution to appreciate this evolution. Results for the loss function and the error estimations can be found in figure 11c and in table C.9.

**3D Navier-Stokes: Beltrami flow (3DNS).** The Beltrami flow is a particular case in fluid mechanics where the vorticity vector  $\mathbf{w} = \nabla \times \mathbf{u}$  is parallel to the velocity vector  $\mathbf{u}$ . This flow satisfies the Navier-Stokes

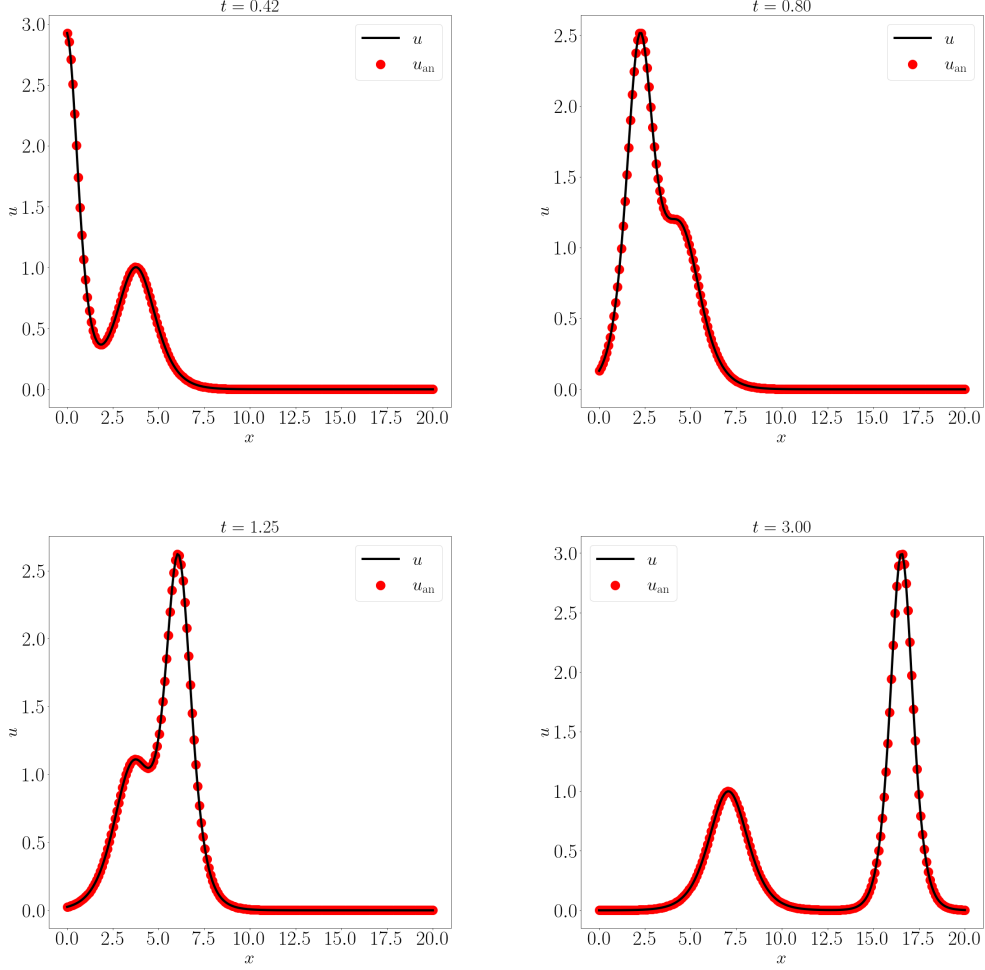


Figure 10: Snapshots of the two-soliton solution (43). Solid black line: PINN approximation. Red dots: analytical solution.

equation for an incompressible fluid:

$$\frac{\partial \mathbf{u}}{\partial t} + (\mathbf{u} \cdot \nabla) \mathbf{u} = -\frac{1}{\rho_0} \nabla p + \nu \nabla^2 \mathbf{u}, \quad (51)$$

$$\nabla \cdot \mathbf{u} = 0, \quad (52)$$

where  $p$  is the pressure,  $\rho_0$  is the (constant) density, and  $\nu$  is the kinematic viscosity. This is a system of four equations for four variables: the three

components of the velocity vector  $\mathbf{u} = (u, v, w)$  and the pressure  $p$ . We solve it in a four dimensional domain in Cartesian coordinates  $x_\alpha = (t, x, y, z)$ . A well-established, non-trivial benchmark for this problem is provided in [43]. We refer the interested reader to that paper to see an illustration of this solution. The three components of the velocity can be written in this case as

$$u = -a [e^{ax} \sin (ay + dz) + e^{az} \cos (ax + dy)] e^{-d^2 t}, \quad (53)$$

$$v = -a [e^{ay} \sin (az + dx) + e^{az} \cos (ay + dz)] e^{-d^2 t}, \quad (54)$$

$$w = -a [e^{az} \sin (ax + dy) + e^{ay} \cos (az + dx)] e^{-d^2 t}. \quad (55)$$

for arbitrary constants  $a, d$ . The solution for the pressure can be written as

$$\begin{aligned} p = -\frac{a^2}{2} [ & e^{2ax} + e^{2ay} + e^{2az} + 2 \sin (ax + dy) \cos (az + dx) e^{a(y+z)} \\ & + 2 \sin (ay + dz) \cos (ax + dy) e^{a(z+x)} \\ & + 2 \sin (az + dx) \cos (ay + dz) e^{a(y+x)}] e^{-2d^2 t}. \end{aligned} \quad (56)$$

In the usual way, we can construct the loss function as the sum of four terms. For each component of equation (51) we have  $\mathcal{L}_i = \frac{\partial}{\partial t} + (\mathbf{u} \cdot \nabla) - \nu \nabla^2$  and  $G = -\frac{1}{\rho_0} \nabla p$ , whereas for equation (52)  $\mathcal{L} = \text{div}$  and  $G = 0$ .

We impose Dirichlet boundary conditions for the three components of the velocity vector  $\mathbf{u}$ . We will describe them for one of them, without loss of generality. If the spatial domain is  $[x_0, x_0 + L_x] \times [y_0, y_0 + L_y] \times [z_0, z_0 + L_z]$ , we define

$$\begin{aligned} f_0(y, z, t) &= u(x_0, y, z, t) - u_0(x_0, y, z), \\ f_1(y, z, t) &= u(x_0 + L_x, y, z, t) - u_0(x_0 + L_x, y, z), \\ g_0(x, z, t) &= u(x, y_0, z, t) - u_0(x, y_0, z), \\ g_1(x, z, t) &= u(x, y_0 + L_y, z, t) - u_0(x, y_0 + L_y, z), \\ h_0(x, y, t) &= u(x, y, z_0, t) - u_0(x, y, z_0), \\ h_1(x, y, t) &= u(x, y, z_0 + L_z, t) - u_0(x, y, z_0 + L_z) \end{aligned}$$

Then, the functions  $f_b$  and  $h_b$  used in (3) can be defined through the the

following ansatz

$$f_b(x, y, z, t) = u_0(x, y, z) + A(x, y, z, t), \quad (57)$$

$$h_b(x, y, z, t) = t \prod_{w=x,y,z} (w - w_0)(w - w_0 - L_w), \quad (58)$$

$$A(x, y, z, t) = (1 - \xi_x) f_0(y, z, t) + \xi_x f_1(y, z, t) + (1 - \xi_y) G_0(x, z, t) + \xi_y G_1(x, z, t) + (1 - \xi_z) H_0(x, y, t) + \xi_z H_1(x, y, t), \quad (59)$$

where  $\xi_q = \frac{q - q_0}{L_q}$  ( $q = x, y, z$ ) and the functions  $\{G_i, H_i\}_{i=0,1}$  are defined as

$$G_i(x, z, t) = g_i(x, t) - (1 - \xi_x) g_i(x_0, t) - \xi_x g_i(x_0 + L_x, t), \quad (60)$$

$$H_i(x, y, t) = h_i(x, y, t) - (1 - \xi_x) h_i(x_0, y, t) - \xi_x h_i(x_0 + L_x, y, t) - (1 - \xi_y) \{h_i(x, y_0, t) - (1 - \xi_x) h_i(x_0, y_0, t) - \xi_x h_i(x_0 + L_x, y_0, t)\} - \xi_y \{h_i(x, y_0 + L_y, t) - (1 - \xi_x) h_i(x_0, y_0 + L_y, t) - \xi_x h_i(x_0 + L_x, y_0 + L_y, t)\}. \quad (61)$$

Regarding the pressure, we only need to specify it at a single spacial point  $(x_1, y_1, z_1)$  for all times  $t$ . This is necessary, because one has the freedom to add a function of time to  $p$  and get an equivalent solution. Indeed, if we replace  $p \rightarrow p + f(t)$  in equation (51) we obtain the same system and the solution is ambiguous. Results for the loss function and the error estimations can be found in figure 11d and table C.10.

#### 4.1. Comparison with the literature

Wrapping up this section, in Table 3 we offer a direct one-to-one comparison of our findings (marked as TW –this work–) presented earlier with similar problems encountered in the PINNs literature (specific references provided in the second column). We utilized the code provided in the GitHub repository cited in [42] for the KdV equation, incorporating the analytical 2-soliton solution and defining the same training domain for this study. As for the NLSE, we employed our code (as the L-BFGS optimizer used in [2] is the same as the one considered here) to compute the corresponding PINN approximation errors defined in 3.2.

In the current landscape of PINN research, L-BFGS has become a widely used optimizer due to its generally superior performance compared to the Adam optimizer. However, it has demonstrated some limitations, especially when confronted with highly ill-conditioned problems, as evidenced in some

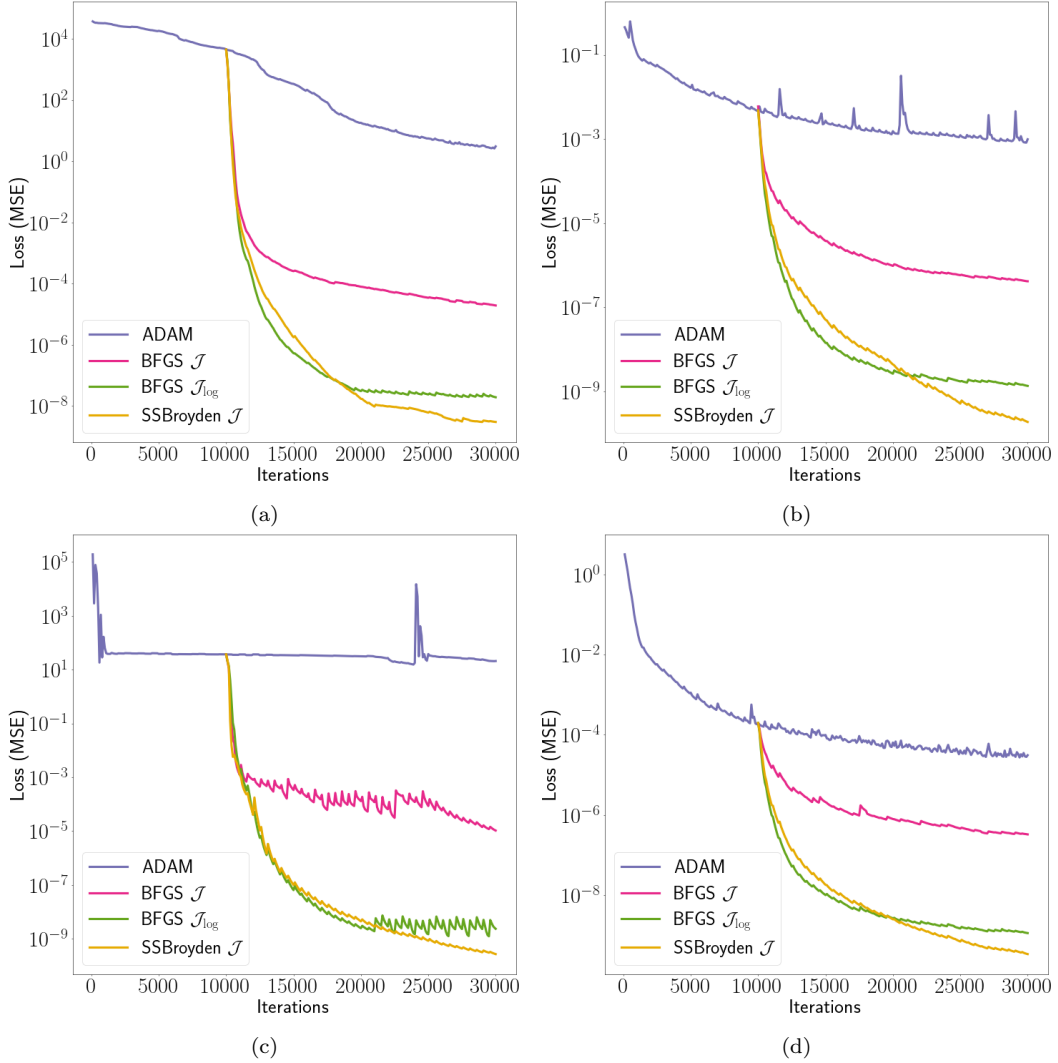


Figure 11: Loss function vs number of iterations for the four problems considered in section 4. Results are obtained by considering Adam with  $\mathcal{J}$ , Adam + BFGS with  $\mathcal{J}$ , Adam + BFGS with  $\mathcal{J}_{\log}$ , and Adam + SSBroyden with  $\mathcal{J}$ . **11a**: Non-linear Poisson equation; **11b**: Non-linear Schrödinger equation; **11c**: KdV equation; **11d**: Navier-Stokes (Beltrami flow) equation.

studies [44]. Consequently, it needs a significantly higher number of trainable parameters than the BFGS algorithm to achieve comparable precision. Naturally, training the identical network with BFGS is markedly slower compared to L-BFGS, primarily due to the former's requirement to store and update

the inverse Hessian estimate at each iteration. However, the ability to utilize smaller networks with BFGS enables obtaining results with comparable or even higher accuracy than those obtained with larger networks with the L-BFGS algorithm.

Figure 12 illustrates this effect. We show the evolution of  $\mathcal{J}$  as a function of the number of iterations (left panel) or training time (right panel) for the NLSE equation. We compare the training process with the L-BFGS and the BFGS algorithms using our smaller neural network (see table 1), and the L-BFGS algorithm with the same NN considered in [2].

As shown by the figure, for identical networks, the L-BFGS algorithm operates approximately four times faster, yet its convergence rate is notably slower. Thus, we note that BFGS proves to be more efficient than L-BFGS for the same number of trainable parameters, both in terms of iterations and training duration. While employing a larger network with L-BFGS enhances accuracy, it does so at the expense of significantly prolonged training periods.

However, the preceding examples in this section illustrate that training with BFGS in conjunction with the MSE loss was not the optimal strategy either. Figure 13 shows again the evolution of  $\mathcal{J}$  as a function of the training time. By introducing modifications to either the BFGS algorithm or the loss function, the performance enhancement becomes even more remarkable. With these adjustments, we observe a reduction of many orders of magnitude in the loss function within the same training duration, compared to L-BFGS. This is directly reflected in the errors achieved in each case, as shown in table 3.

## 5. Conclusions.

In this study, we have investigated the boundaries of accuracy achievable by physics-informed neural networks (PINNs). Unlike conventional methods, which benefit from a solid mathematical foundation (built over many decades) offering insights into methodological order and accuracy constraints, the young field of PINNs usually relies on a brute force methodology involving trial and error. We emphasize the pivotal significance of the optimization algorithm in attaining robust convergence, irrespective of the specific physical problem. Furthermore, we demonstrate how making appropriate selections can substantially enhance result accuracy by several orders of magnitude, independently of the specific physical problem being addressed.

Problem	Reference	Optimizer	Loss	Layers	Neurons	Error
$E_\phi$						
NLP ( $k = 1$ )	[27]	L-BFGS	$\mathcal{J}$	4	50	$1.08 \times 10^{-6}$
	TW	BFGS	$\mathcal{J}$	2	30	$7.65 \times 10^{-7}$
	TW	SSBroyden	$\mathcal{J}$	2	40	$4.60 \times 10^{-9}$
	TW	BFGS	$\mathcal{J}_{\log}$	2	40	$6.86 \times 10^{-9}$
$(\epsilon_{\text{NN}}^{(u)}, \epsilon_{\text{NN}}^{(v)})$						
NLS	[2]	L-BFGS	$\mathcal{J}$	4	100	$(2.23, 2.05) \times 10^{-3}$
	TW	BFGS	$\mathcal{J}$	2	40	$(4.32, 4.16) \times 10^{-4}$
	TW	SSBroyden	$\mathcal{J}$	2	40	$(2.42, 2.40) \times 10^{-5}$
	TW	BFGS	$\mathcal{J}_{\log}$	2	40	$(3.85, 3.38) \times 10^{-5}$
$E_u$						
KdV	[42]	L-BFGS	$\mathcal{J}$	4	32	$1.07 \times 10^{-2}$
	[42]	L-BFGS	$\mathcal{J}$	8	60	$1.26 \times 10^{-3}$
	TW	BFGS	$\mathcal{J}$	3	30	$4.16 \times 10^{-4}$
	TW	SSBroyden	$\mathcal{J}$	3	30	$6.74 \times 10^{-6}$
	TW	BFGS	$\mathcal{J}_{\log}$	3	30	$1.22 \times 10^{-5}$
$(E_u, E_v, E_w)$						
3DNS	[45]	L-BFGS	$\mathcal{J}$	7	50	$(2.54, 2.40, 2.60) \times 10^{-4}$
	TW	BFGS	$\mathcal{J}$	2	40	$(1.30, 1.59, 1.63) \times 10^{-5}$
	TW	SSBroyden	$\mathcal{J}$	2	40	$(7.24, 7.07, 7.78) \times 10^{-7}$
	TW	BFGS	$\mathcal{J}_{\log}$	2	40	$(1.27, 1.36, 1.33) \times 10^{-6}$

Table 3: Comparison between models in the literature (references in the second column) and our models (this work TW) trained with our optimizer and loss function modifications. If an analytical solution exists, we compute the error as the  $L_2$  relative norm, denoted for a given solution  $u$  by  $E_u$ . If not (as in the non-linear Schrödinger equation), we compute the PINN approximation error  $\epsilon_{\text{NN}}$  defined in (3.2).

In the family of quasi-Newton methods, the convergence rate of each algorithm is linked to the well-conditioning of the corresponding Hessian matrix  $\text{hess}(\mathcal{J}(\mathbf{z}))$ . We have demonstrated that, when the eigenvalue spectrum of  $\text{hess}(\mathcal{J}(\mathbf{z}))$  is centered around unity with minimal dispersion, the optimization process efficiently minimizes the loss function, resulting in highly precise solutions. A similar effect is produced by considering a modified loss



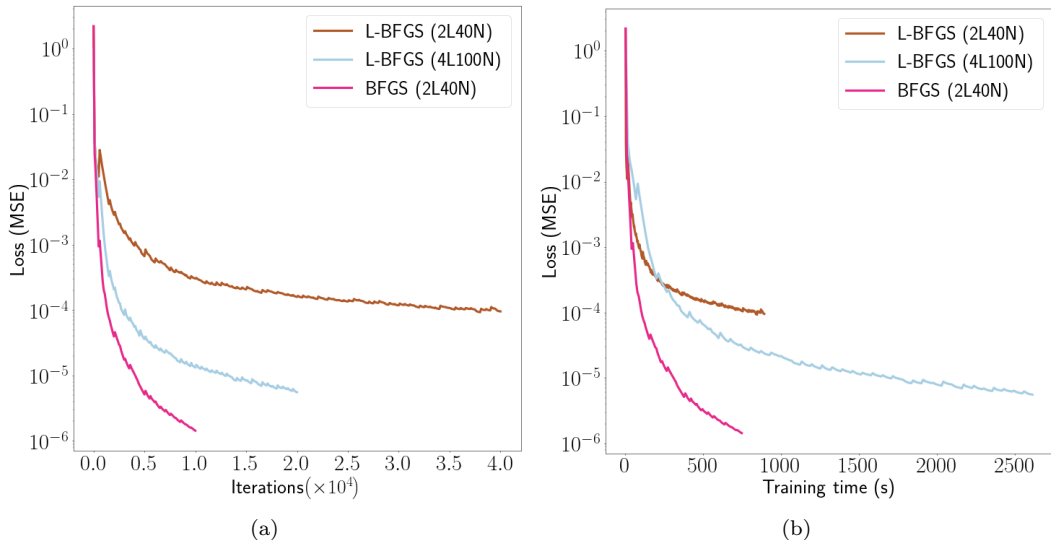


Figure 12: Loss function obtained for the NLSE equation considering the L-BFGS and BFGS algorithms with the network employed in this work (2L40N) for this particular problem (see table 1) and the L-BFGS algorithm for the model suggested in [2] (4L100N), as a function of the number of iterations (12a) and the training time (12b).

function  $\mathcal{J}_g$  instead of the usual MSE loss. Changes to the loss function can be paired with selecting an optimization algorithm, enabling thorough exploration of different combinations. Our research suggests that the optimization algorithm choice typically has a greater effect on convergence compared to adjustments to the loss function. However, the ease of implementation may favor employing modifications to the loss function for practical purposes: very often it is much easier to tweak the loss function than to either change an existing optimizer or create a new one entirely.

However, as the field of PINNs continues to evolve and we gain a deeper understanding of the optimization process underlying neural network training, more sophisticated algorithms will likely become readily available in popular machine learning frameworks. This study also seeks to encourage developers to move in this direction.

A crucial result of refining the optimization process in PINNs is the significant reduction in both the size and complexity of the networks used to tackle similar problems. Through our series of benchmarks, we have demonstrated how various problems from the literature can be solved with notably smaller network sizes and improved precision, as illustrated in Table 3. This

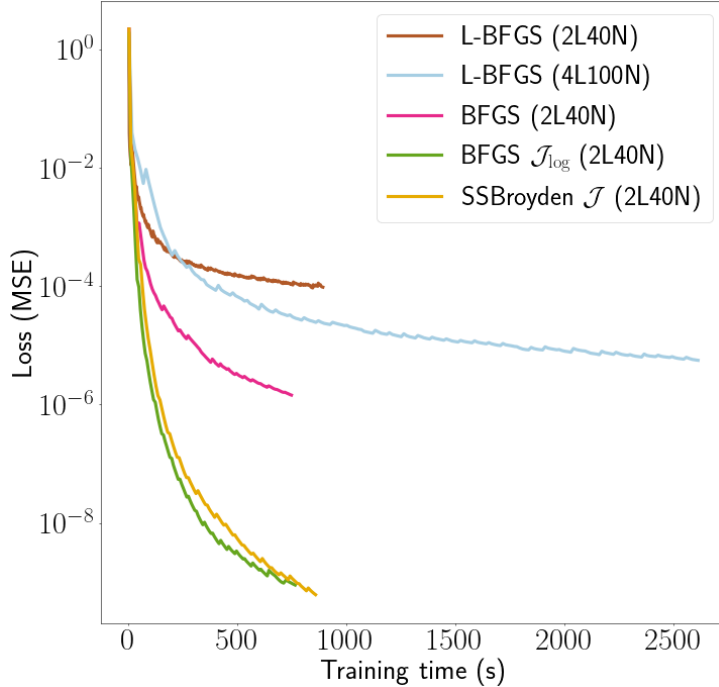


Figure 13: Loss function vs. training time for the NLSE equation obtained with our training process modifications. The ones presented in figure 12b are also shown for reference.

enhances numerical efficiency, addressing a key weakness of PINNs compared to classical numerical methods.

Indeed, all simulations presented in this study were conducted on a standard PC or, in some cases, on a regular laptop, without any specialized requirements. While enhancements to other hyperparameters such as activation functions and network structure can provide further assistance, our primary finding underscores the crucial importance of leveraging improved optimizers and rescaled loss functions. We anticipate that this effect will become even more significant as the problem’s dimensionality increases, especially when addressing large-scale problems.

Currently, the most frequently employed optimizer in PINNs is the L-BFGS algorithm, which is a faster variant of BFGS (per iteration) but suffers even more from ill-conditioning. As a consequence, the latter needs much more trainable parameters to obtain results of similar accuracy. As future work, we will explore how the different modifications of the L-BFGS algorithm suggested in optimization theory literature affect the convergence in

PINNs.

## Acknowledgments

We acknowledge the support through the grant PID2021-127495NB-I00 funded by MCIN/AEI/10.13039/501100011033 and by the European Union, the Astrophysics and High Energy Physics programme of the Generalitat Valenciana ASFAE/2022/026 funded by MCIN and the European Union NextGenerationEU (PRTR-C17.I1) and the Prometeo excellence programme grant CIPROM/2022/13. JFU is supported by the predoctoral fellowship ACIF 2023, cofunded by Generalitat Valenciana and the European Union through the European Social Fund.

## Appendix A. Efficient computation of the scaling parameter $\tau_k^{(1)}$

The computation of inverse matrices should be avoided, since it is  $\mathcal{O}(n^3)$  and also is a potential source of numerical errors if  $H_k$  is ill-conditioned. Instead, note that from (5), (6) and (7) we can write

$$H_k^{-1} \mathbf{s}_k = -\alpha_k \nabla \mathcal{J}(\Theta_k), \quad (\text{A.1})$$

so the explicit dependence of  $\tau_k^{(1)}$  on  $H_k^{-1}$  disappears. The step length  $\alpha_k$  and the gradient  $\nabla \mathcal{J}(\Theta_k)$  are available at iteration  $k$  so there is no problem in evaluating the latter expression. Hence, the calculation of the scaling parameter only involves vector multiplications, which is  $\mathcal{O}(n)$ , as

$$\tau_k^{(1)} = \min \left\{ 1, \frac{-\mathbf{y}_k \cdot \mathbf{s}_k}{\alpha_k \mathbf{s}_k \cdot \nabla \mathcal{J}(\Theta_k)} \right\}, \quad (\text{A.2})$$

Note that the original suggestion of [18] for the scaling parameter was simply  $\tau_k^{(1)} = \frac{-\mathbf{y}_k \cdot \mathbf{s}_k}{\alpha_k \mathbf{s}_k \cdot \nabla \mathcal{J}(\Theta_k)}$ , which was indeed motivated by the need to reduce the condition number of (24). However, this choice has shown to be inferior in terms of performance compared to the standard BFGS, when combined with an inexact line search computation of  $\alpha_k$ , as shown in [46] and was confirmed by our own analysis. Instead, we followed the suggestion introduced in [17], which is a simple modification of the original one, but ensures theoretically super-linear convergence with inexact line searches. In fact, it can be thought as a switch between the standard BFGS algorithm ( $\tau_k = 1$ ) and the self-scaled BFGS algorithm of [18]. Curiously, we found that in the majority

of the training iterations, the value of  $\tau_k = 1$  is selected, with only a small portion of them benefitting from the scaling. Still, this was sufficient to produce considerable improvements in the optimization process.

## Appendix B. Self-scaled Broyden optimization algorithm

The intermediate variables  $\theta_k$ ,  $\sigma_k$  and  $a_k$  defined in [15] and used in equations (20), (21) are given by

$$b_k = \frac{\mathbf{s}_k \cdot H_k^{-1} \mathbf{s}_k}{\mathbf{y}_k \cdot \mathbf{s}_k} = -\alpha_k \frac{\mathbf{s}_k \cdot \nabla \mathcal{J}(\Theta_k)}{\mathbf{y}_k \cdot \mathbf{s}_k}, \quad (\text{B.1})$$

$$h_k = \frac{\mathbf{y}_k \cdot H_k \mathbf{y}_k}{\mathbf{y}_k \cdot \mathbf{s}_k}, \quad (\text{B.2})$$

$$a_k = h_k b_k - 1 \quad (\text{B.3})$$

$$c_k = \sqrt{\frac{a_k}{a_k + 1}}, \quad (\text{B.4})$$

$$\rho_k^- = \min(1, h_k(1 - c_k)), \quad (\text{B.5})$$

$$\theta_k^- = \frac{\rho_k^- - 1}{a_k}, \quad (\text{B.6})$$

$$\theta_k^+ = \frac{1}{\rho_k^-}, \quad (\text{B.7})$$

$$\theta_k = \max\left(\theta_k^-, \min\left(\theta_k^+, \frac{b_k}{1 - b_k}\right)\right) \quad (\text{B.8})$$

$$\sigma_k = 1 + a_k \theta_k. \quad (\text{B.9})$$

## Appendix C. Error analysis

We present tables with error measurements for the various problems that we solve.

For each problem, we repeat the training process for each modification of the optimization algorithm or the loss function using different random initialization for the trainable parameters and the training set. The experiments are labeled with a particular number, indicating a given seed for the random number generator. We calculate the final value of the MSE loss and the errors measured in a given set of tests points. If there exists an analytical

solution to the problem, say  $u_{\text{an}}$ , then we define the error of order  $p$  at the PINN approximation  $u$  as

$$E_u^{(p)} = \frac{\|u - u_{\text{an}}\|_p}{\|u_{\text{an}}\|_p}, \quad (\text{C.1})$$

where  $\|\cdot\|_p$  indicates the norm of order  $p$ . If not, we provide  $\epsilon_{\text{NN}}$  as a global estimation of the PINN approximation error, together with an illustrative plot of  $\epsilon_{\text{FD}}$  as a function of the resolution  $N_0$ .

Exp.	$(\tau_k, \phi_k)$	$\mathcal{J}$	$E_{\mathcal{P}}^{(1)}$	$E_{\mathcal{P}}^{(2)}$	$E_{B_r}^{(1)}$	$E_{B_r}^{(2)}$	$E_{B_\theta}^{(1)}$	$E_{B_\theta}^{(2)}$
1	(1, 1)	$1.69 \times 10^{-8}$	$2.34 \times 10^{-6}$	$2.09 \times 10^{-6}$	$1.16 \times 10^{-5}$	$1.29 \times 10^{-5}$	$6.36 \times 10^{-6}$	$6.34 \times 10^{-6}$
2	(1, 1)	$1.40 \times 10^{-8}$	$1.86 \times 10^{-6}$	$1.81 \times 10^{-6}$	$8.38 \times 10^{-6}$	$8.59 \times 10^{-6}$	$6.13 \times 10^{-6}$	$6.57 \times 10^{-6}$
3	(1, 1)	$6.23 \times 10^{-8}$	$3.45 \times 10^{-6}$	$3.38 \times 10^{-6}$	$2.88 \times 10^{-5}$	$4.09 \times 10^{-5}$	$1.15 \times 10^{-5}$	$1.15 \times 10^{-5}$
4	(1, 1)	$4.75 \times 10^{-8}$	$5.45 \times 10^{-6}$	$5.05 \times 10^{-6}$	$2.30 \times 10^{-5}$	$2.74 \times 10^{-5}$	$1.22 \times 10^{-5}$	$1.36 \times 10^{-5}$
5	(1, 1)	$1.41 \times 10^{-8}$	$1.55 \times 10^{-6}$	$1.46 \times 10^{-6}$	$1.20 \times 10^{-5}$	$1.55 \times 10^{-5}$	$5.06 \times 10^{-6}$	$5.17 \times 10^{-6}$
Mean	(1, 1)	<b><math>3.10 \times 10^{-8}</math></b>	<b><math>2.92 \times 10^{-6}</math></b>	<b><math>2.76 \times 10^{-6}</math></b>	<b><math>1.68 \times 10^{-5}</math></b>	<b><math>2.11 \times 10^{-5}</math></b>	<b><math>8.25 \times 10^{-6}</math></b>	<b><math>8.63 \times 10^{-6}</math></b>
1	$(\tau_k^{(1)}, 1)$	$2.33 \times 10^{-10}$	$2.72 \times 10^{-7}$	$2.56 \times 10^{-7}$	$2.17 \times 10^{-6}$	$3.24 \times 10^{-6}$	$5.65 \times 10^{-7}$	$3.86 \times 10^{-7}$
2	$(\tau_k^{(1)}, 1)$	$1.07 \times 10^{-10}$	$1.65 \times 10^{-7}$	$1.50 \times 10^{-7}$	$1.33 \times 10^{-6}$	$1.91 \times 10^{-6}$	$4.82 \times 10^{-7}$	$5.07 \times 10^{-7}$
3	$(\tau_k^{(1)}, 1)$	$4.48 \times 10^{-11}$	$1.55 \times 10^{-7}$	$1.49 \times 10^{-7}$	$9.11 \times 10^{-7}$	$1.36 \times 10^{-6}$	$3.35 \times 10^{-7}$	$3.58 \times 10^{-7}$
4	$(\tau_k^{(1)}, 1)$	$1.68 \times 10^{-10}$	$1.91 \times 10^{-7}$	$1.98 \times 10^{-7}$	$1.81 \times 10^{-6}$	$2.82 \times 10^{-6}$	$4.82 \times 10^{-7}$	$4.74 \times 10^{-7}$
5	$(\tau_k^{(1)}, 1)$	$1.03 \times 10^{-10}$	$2.01 \times 10^{-7}$	$1.97 \times 10^{-7}$	$1.40 \times 10^{-6}$	$2.08 \times 10^{-6}$	$4.14 \times 10^{-7}$	$3.86 \times 10^{-7}$
Mean	$(\tau_k^{(1)}, 1)$	<b><math>1.32 \times 10^{-10}</math></b>	<b><math>1.97 \times 10^{-7}</math></b>	<b><math>1.90 \times 10^{-7}</math></b>	<b><math>1.53 \times 10^{-6}</math></b>	<b><math>2.28 \times 10^{-6}</math></b>	<b><math>4.56 \times 10^{-7}</math></b>	<b><math>4.50 \times 10^{-7}</math></b>
1	$(\tau_k^{(2)}, \phi_k^{(1)})$	$4.48 \times 10^{-11}$	$1.36 \times 10^{-7}$	$1.32 \times 10^{-7}$	$8.76 \times 10^{-7}$	$1.23 \times 10^{-6}$	$2.88 \times 10^{-7}$	$2.86 \times 10^{-7}$
2	$(\tau_k^{(2)}, \phi_k^{(1)})$	$1.88 \times 10^{-11}$	$6.59 \times 10^{-8}$	$6.31 \times 10^{-8}$	$4.12 \times 10^{-7}$	$5.34 \times 10^{-7}$	$1.46 \times 10^{-7}$	$1.42 \times 10^{-7}$
3	$(\tau_k^{(2)}, \phi_k^{(1)})$	$4.42 \times 10^{-11}$	$9.81 \times 10^{-8}$	$1.06 \times 10^{-7}$	$8.97 \times 10^{-7}$	$1.38 \times 10^{-6}$	$3.01 \times 10^{-7}$	$3.48 \times 10^{-7}$
4	$(\tau_k^{(2)}, \phi_k^{(1)})$	$2.96 \times 10^{-11}$	$1.20 \times 10^{-7}$	$1.08 \times 10^{-7}$	$6.86 \times 10^{-7}$	$1.02 \times 10^{-6}$	$2.58 \times 10^{-7}$	$2.75 \times 10^{-7}$
5	$(\tau_k^{(2)}, \phi_k^{(1)})$	$2.46 \times 10^{-11}$	$1.22 \times 10^{-7}$	$1.13 \times 10^{-7}$	$7.94 \times 10^{-7}$	$1.23 \times 10^{-6}$	$1.68 \times 10^{-7}$	$1.86 \times 10^{-7}$
Mean	$(\tau_k^{(2)}, \phi_k^{(1)})$	<b><math>3.24 \times 10^{-11}</math></b>	<b><math>1.08 \times 10^{-7}</math></b>	<b><math>1.04 \times 10^{-7}</math></b>	<b><math>7.33 \times 10^{-7}</math></b>	<b><math>1.07 \times 10^{-6}</math></b>	<b><math>2.32 \times 10^{-7}</math></b>	<b><math>2.48 \times 10^{-7}</math></b>

Table C.4: Final loss values and error norms associated with  $\mathcal{P}$  and with the magnetic field components  $(B_r, B_\theta)$ , obtained with the standard BFGS (1, 1), the self-scaled BFGS  $(\tau_k^{(1)}, 0)$  and the self-scaled Broyden updates  $(\tau_k^{(2)}, \phi_k^{(1)})$ , for the current-free dipole-quadrupole case.

Exp.	Loss	$\mathcal{J}$	$E_{\mathcal{P}}^{(1)}$	$E_{\mathcal{P}}^{(2)}$	$E_{B_r}^{(1)}$	$E_{B_r}^{(2)}$	$E_{B_\theta}^{(1)}$	$E_{B_\theta}^{(2)}$
1	$\mathcal{J}$	$1.69 \times 10^{-8}$	$2.34 \times 10^{-6}$	$2.09 \times 10^{-6}$	$1.16 \times 10^{-5}$	$1.29 \times 10^{-5}$	$6.36 \times 10^{-6}$	$6.34 \times 10^{-6}$
2	$\mathcal{J}$	$1.40 \times 10^{-8}$	$1.86 \times 10^{-6}$	$1.81 \times 10^{-6}$	$8.38 \times 10^{-6}$	$8.59 \times 10^{-6}$	$6.13 \times 10^{-6}$	$6.57 \times 10^{-6}$
3	$\mathcal{J}$	$6.23 \times 10^{-8}$	$3.45 \times 10^{-6}$	$3.38 \times 10^{-6}$	$2.88 \times 10^{-5}$	$4.09 \times 10^{-5}$	$1.15 \times 10^{-5}$	$1.15 \times 10^{-5}$
4	$\mathcal{J}$	$4.75 \times 10^{-8}$	$5.45 \times 10^{-6}$	$5.05 \times 10^{-6}$	$2.30 \times 10^{-5}$	$2.74 \times 10^{-5}$	$1.22 \times 10^{-5}$	$1.36 \times 10^{-5}$
5	$\mathcal{J}$	$1.41 \times 10^{-8}$	$1.55 \times 10^{-6}$	$1.46 \times 10^{-6}$	$1.20 \times 10^{-5}$	$1.55 \times 10^{-5}$	$5.06 \times 10^{-6}$	$5.17 \times 10^{-6}$
Mean	$\mathcal{J}$	<b><math>3.10 \times 10^{-8}</math></b>	<b><math>2.92 \times 10^{-6}</math></b>	<b><math>2.76 \times 10^{-6}</math></b>	<b><math>1.68 \times 10^{-5}</math></b>	<b><math>2.11 \times 10^{-5}</math></b>	<b><math>8.25 \times 10^{-6}</math></b>	<b><math>8.63 \times 10^{-6}</math></b>
1	$\mathcal{J}_{1/2}$	$5.79 \times 10^{-10}$	$4.21 \times 10^{-7}$	$4.12 \times 10^{-7}$	$3.49 \times 10^{-6}$	$5.49 \times 10^{-6}$	$1.18 \times 10^{-6}$	$1.22 \times 10^{-6}$
2	$\mathcal{J}_{1/2}$	$3.26 \times 10^{-10}$	$2.64 \times 10^{-7}$	$2.65 \times 10^{-7}$	$1.48 \times 10^{-6}$	$1.57 \times 10^{-6}$	$1.18 \times 10^{-6}$	$1.31 \times 10^{-6}$
3	$\mathcal{J}_{1/2}$	$8.33 \times 10^{-10}$	$4.84 \times 10^{-7}$	$4.79 \times 10^{-7}$	$3.48 \times 10^{-6}$	$4.89 \times 10^{-6}$	$1.40 \times 10^{-6}$	$1.31 \times 10^{-6}$
4	$\mathcal{J}_{1/2}$	$9.87 \times 10^{-10}$	$4.45 \times 10^{-7}$	$4.18 \times 10^{-7}$	$4.00 \times 10^{-6}$	$5.72 \times 10^{-6}$	$1.39 \times 10^{-6}$	$1.40 \times 10^{-6}$
5	$\mathcal{J}_{1/2}$	$2.40 \times 10^{-10}$	$2.35 \times 10^{-7}$	$2.41 \times 10^{-7}$	$1.84 \times 10^{-6}$	$2.44 \times 10^{-6}$	$5.95 \times 10^{-7}$	$5.79 \times 10^{-7}$
Mean	$\mathcal{J}_{1/2}$	<b><math>5.93 \times 10^{-10}</math></b>	<b><math>3.70 \times 10^{-7}</math></b>	<b><math>3.63 \times 10^{-7}</math></b>	<b><math>2.86 \times 10^{-6}</math></b>	<b><math>4.02 \times 10^{-6}</math></b>	<b><math>1.15 \times 10^{-6}</math></b>	<b><math>1.17 \times 10^{-6}</math></b>
1	$\mathcal{J}_{\log}$	$9.19 \times 10^{-11}$	$1.09 \times 10^{-7}$	$1.03 \times 10^{-7}$	$1.13 \times 10^{-6}$	$1.66 \times 10^{-6}$	$3.93 \times 10^{-7}$	$3.99 \times 10^{-7}$
2	$\mathcal{J}_{\log}$	$9.50 \times 10^{-11}$	$1.52 \times 10^{-7}$	$1.44 \times 10^{-7}$	$1.09 \times 10^{-6}$	$1.38 \times 10^{-6}$	$4.25 \times 10^{-7}$	$4.14 \times 10^{-7}$
3	$\mathcal{J}_{\log}$	$3.42 \times 10^{-10}$	$3.05 \times 10^{-7}$	$2.92 \times 10^{-7}$	$2.33 \times 10^{-6}$	$3.16 \times 10^{-6}$	$8.17 \times 10^{-7}$	$7.69 \times 10^{-7}$
4	$\mathcal{J}_{\log}$	$6.33 \times 10^{-10}$	$3.66 \times 10^{-7}$	$3.64 \times 10^{-7}$	$2.83 \times 10^{-6}$	$3.85 \times 10^{-6}$	$1.11 \times 10^{-7}$	$1.17 \times 10^{-6}$
5	$\mathcal{J}_{\log}$	$2.62 \times 10^{-10}$	$2.73 \times 10^{-7}$	$2.52 \times 10^{-7}$	$1.63 \times 10^{-6}$	$2.01 \times 10^{-6}$	$9.87 \times 10^{-7}$	$1.01 \times 10^{-6}$
Mean	$\mathcal{J}_{\log}$	<b><math>2.85 \times 10^{-10}</math></b>	<b><math>2.41 \times 10^{-7}</math></b>	<b><math>2.31 \times 10^{-7}</math></b>	<b><math>1.80 \times 10^{-6}</math></b>	<b><math>2.41 \times 10^{-6}</math></b>	<b><math>7.47 \times 10^{-7}</math></b>	<b><math>7.55 \times 10^{-7}</math></b>

Table C.5: Final loss values and error norms associated with  $\mathcal{P}$  and with the magnetic field components  $(B_r, B_\theta)$  obtained with the standard BFGS (1,1) in conjunction with the loss function modifications defined in (27), (28) for the current-free dipole-quadrupole case.

(a)			(b)		
Exp.	$(\tau_k, \phi_k)$	$\epsilon_{\text{NN}}$	Exp.	Loss	$\epsilon_{\text{NN}}$
1	(1, 1)	$1.57 \times 10^{-3}$	1	$\mathcal{J}$	$1.57 \times 10^{-3}$
2	(1, 1)	$1.53 \times 10^{-3}$	2	$\mathcal{J}$	$1.53 \times 10^{-3}$
3	(1, 1)	$1.98 \times 10^{-3}$	3	$\mathcal{J}$	$1.98 \times 10^{-3}$
4	(1, 1)	$1.93 \times 10^{-3}$	4	$\mathcal{J}$	$1.93 \times 10^{-3}$
5	(1, 1)	$1.77 \times 10^{-3}$	5	$\mathcal{J}$	$1.77 \times 10^{-3}$
Mean	(1, 1)	<b><math>1.76 \times 10^{-3}</math></b>	Mean	$\mathcal{J}$	<b><math>1.76 \times 10^{-3}</math></b>
1	$(\tau_k^{(1)}, 1)$	$3.45 \times 10^{-5}$	1	$\mathcal{J}_{1/2}$	$4.77 \times 10^{-4}$
2	$(\tau_k^{(1)}, 1)$	$5.42 \times 10^{-5}$	2	$\mathcal{J}_{1/2}$	$3.10 \times 10^{-4}$
3	$(\tau_k^{(1)}, 1)$	$5.39 \times 10^{-5}$	3	$\mathcal{J}_{1/2}$	$4.06 \times 10^{-4}$
4	$(\tau_k^{(1)}, 1)$	$2.47 \times 10^{-5}$	4	$\mathcal{J}_{1/2}$	$2.79 \times 10^{-4}$
5	$(\tau_k^{(1)}, 1)$	$3.15 \times 10^{-5}$	5	$\mathcal{J}_{1/2}$	$4.14 \times 10^{-4}$
Mean	$(\tau_k^{(1)}, 1)$	<b><math>3.98 \times 10^{-5}</math></b>	Mean	$\mathcal{J}_{1/2}$	<b><math>3.98 \times 10^{-4}</math></b>
1	$(\tau_k^{(2)}, \phi_k^{(1)})$	$1.45 \times 10^{-5}$	1	$\mathcal{J}_{\log}$	$6.68 \times 10^{-5}$
2	$(\tau_k^{(2)}, \phi_k^{(1)})$	$1.84 \times 10^{-5}$	2	$\mathcal{J}_{\log}$	$5.40 \times 10^{-5}$
3	$(\tau_k^{(2)}, \phi_k^{(1)})$	$1.44 \times 10^{-5}$	3	$\mathcal{J}_{\log}$	$9.29 \times 10^{-5}$
4	$(\tau_k^{(2)}, \phi_k^{(1)})$	$1.29 \times 10^{-5}$	4	$\mathcal{J}_{\log}$	$1.33 \times 10^{-4}$
5	$(\tau_k^{(2)}, \phi_k^{(1)})$	$1.51 \times 10^{-5}$	5	$\mathcal{J}_{\log}$	$2.97 \times 10^{-5}$
Mean	$(\tau_k^{(2)}, \phi_k^{(1)})$	<b><math>1.51 \times 10^{-5}</math></b>	Mean	$\mathcal{J}_{\log}$	<b><math>6.93 \times 10^{-5}</math></b>

Table C.6: Values of  $\epsilon_{\text{NN}}$  obtained for the eight multipoles force-free solution. In C.6a they are calculated by considering the BFGS modifications together with the standard MSE loss  $\mathcal{J}$ , whereas in C.6b by considering the loss function modifications in conjunction with the standard BFGS algorithm.

Exp.	$(\tau_k, \phi_k)$	$\mathcal{J}$	$E_\phi^{(2)}$
1	(1, 1)	$\mathcal{J}$	$1.71 \times 10^{-6}$
2	(1, 1)	$\mathcal{J}$	$2.55 \times 10^{-6}$
3	(1, 1)	$\mathcal{J}$	$2.06 \times 10^{-6}$
Mean	(1, 1)	$\mathcal{J}$	<b><math>2.11 \times 10^{-6}</math></b>
Exp.	$(\tau_k, \phi_k)$	$\mathcal{J}_{\log}$	$E_\phi^{(2)}$
1	(1, 1)	$\mathcal{J}_{\log}$	$1.69 \times 10^{-8}$
2	(1, 1)	$\mathcal{J}_{\log}$	$7.81 \times 10^{-8}$
3	(1, 1)	$\mathcal{J}_{\log}$	$7.60 \times 10^{-8}$
Mean	(1, 1)	$\mathcal{J}_{\log}$	<b><math>5.70 \times 10^{-8}</math></b>
Exp.	$(\tau_k^{(2)}, \phi_k^{(1)})$	$\mathcal{J}$	$E_\phi^{(2)}$
1	$(\tau_k^{(2)}, \phi_k^{(1)})$	$\mathcal{J}$	$1.91 \times 10^{-8}$
2	$(\tau_k^{(2)}, \phi_k^{(1)})$	$\mathcal{J}$	$3.52 \times 10^{-8}$
3	$(\tau_k^{(2)}, \phi_k^{(1)})$	$\mathcal{J}$	$4.75 \times 10^{-8}$
Mean	$(\tau_k^{(2)}, \phi_k^{(1)})$	$\mathcal{J}$	<b><math>3.39 \times 10^{-8}</math></b>

Table C.7: Values of  $\epsilon_{\text{NN}}$  obtained with the standard BFGS (1, 1), the self-scaled BFGS  $(\tau_k^{(1)}, 0)$  and the self-scaled Broyden updates  $(\tau_k^{(2)}, \phi_k^{(1)})$ , for the Non-linear Poisson solution.

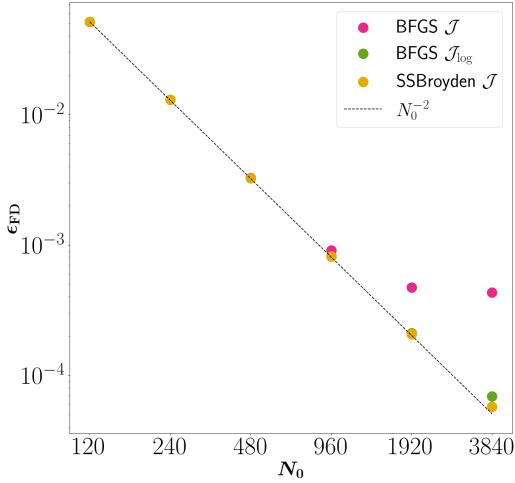


Figure C.14:  $\epsilon_{\text{FD}}$  as a function of the resolution  $N_0$  for the equation (38). A very similar trend is also obtained for the equation (39)

Exp.	$(\tau_k, \phi_k)$	Loss	$\epsilon_{\text{NN}}$ (38)	$\epsilon_{\text{NN}}$ (39)
1	(1, 1)	$\mathcal{J}$	$3.89 \times 10^{-4}$	$3.57 \times 10^{-4}$
2	(1, 1)	$\mathcal{J}$	$4.54 \times 10^{-4}$	$4.19 \times 10^{-4}$
3	(1, 1)	$\mathcal{J}$	$4.32 \times 10^{-4}$	$4.15 \times 10^{-4}$
Mean	(1, 1)	$\mathcal{J}$	<b><math>4.25 \times 10^{-4}</math></b>	<b><math>3.97 \times 10^{-4}</math></b>
Exp.	$(\tau_k, \phi_k)$	Loss	$\epsilon_{\text{NN}}$ (38)	$\epsilon_{\text{NN}}$ (39)
1	(1, 1)	$\mathcal{J}_{\log}$	$3.84 \times 10^{-5}$	$3.38 \times 10^{-5}$
2	(1, 1)	$\mathcal{J}_{\log}$	$3.65 \times 10^{-5}$	$3.25 \times 10^{-5}$
3	(1, 1)	$\mathcal{J}_{\log}$	$4.34 \times 10^{-5}$	$3.69 \times 10^{-5}$
Mean	(1, 1)	$\mathcal{J}_{\log}$	<b><math>3.94 \times 10^{-5}</math></b>	<b><math>3.34 \times 10^{-5}</math></b>
Exp.	$(\tau_k^{(2)}, \phi_k^{(1)})$	Loss	$\epsilon_{\text{NN}}$ (38)	$\epsilon_{\text{NN}}$ (39)
1	$(\tau_k^{(2)}, \phi_k^{(1)})$	$\mathcal{J}$	$2.66 \times 10^{-5}$	$2.17 \times 10^{-5}$
2	$(\tau_k^{(2)}, \phi_k^{(1)})$	$\mathcal{J}$	$1.54 \times 10^{-5}$	$1.32 \times 10^{-5}$
3	$(\tau_k^{(2)}, \phi_k^{(1)})$	$\mathcal{J}$	$2.42 \times 10^{-5}$	$2.41 \times 10^{-5}$
Mean	$(\tau_k^{(2)}, \phi_k^{(1)})$	$\mathcal{J}$	<b><math>2.20 \times 10^{-5}</math></b>	<b><math>1.96 \times 10^{-5}</math></b>

Table C.8: Values of  $\epsilon_{\text{NN}}$  obtained for the non-linear Schrödinger equation, considering the standard BFGS algorithm with  $\mathcal{J}$ , the standard BFGS algorithm with  $\mathcal{J}_{\log}$ , and the self-scaled Broyden algorithm with  $\mathcal{J}$ .



Exp.	$(\tau_k, \phi_k)$	$\mathcal{J}$	$E_u^{(2)}$
1	(1, 1)	$\mathcal{J}$	$1.97 \times 10^{-4}$
2	(1, 1)	$\mathcal{J}$	$1.43 \times 10^{-4}$
3	(1, 1)	$\mathcal{J}$	$9.08 \times 10^{-4}$
Mean	(1, 1)	$\mathcal{J}$	<b><math>4.16 \times 10^{-4}</math></b>
1	(1, 1)	$\mathcal{J}_{\log}$	$1.43 \times 10^{-5}$
2	(1, 1)	$\mathcal{J}_{\log}$	$1.44 \times 10^{-5}$
3	(1, 1)	$\mathcal{J}_{\log}$	$7,84 \times 10^{-6}$
Mean	(1, 1)	$\mathcal{J}_{\log}$	<b><math>1.22 \times 10^{-5}</math></b>
1	$\left(\tau_k^{(2)}, \phi_k^{(1)}\right)$	$\mathcal{J}$	$7.26 \times 10^{-6}$
2	$\left(\tau_k^{(2)}, \phi_k^{(1)}\right)$	$\mathcal{J}$	$7.00 \times 10^{-6}$
3	$\left(\tau_k^{(2)}, \phi_k^{(1)}\right)$	$\mathcal{J}$	$5,96 \times 10^{-6}$
Mean	$\left(\tau_k^{(2)}, \phi_k^{(1)}\right)$	$\mathcal{J}$	<b><math>6.74 \times 10^{-6}</math></b>

Table C.9: Error norms of the PINN approximation for the KdV two soliton solution, obtained with the standard BFGS and the MSE loss, with the standard BFGS and  $\mathcal{J}_{\log}$  defined at (28), and with the self-scaled Broyden updates  $(\tau_k^{(2)}, \phi_k^{(1)})$  in conjunction with the MSE loss.

Exp.	$(\tau_k, \phi_k)$	Loss	$E_u^{(2)}$	$E_v^{(2)}$	$E_w^{(2)}$	$E_p^{(2)}$
1	(1, 1)	$\mathcal{J}$	$1.23 \times 10^{-5}$	$1.56 \times 10^{-5}$	$1.44 \times 10^{-5}$	$1.08 \times 10^{-4}$
2	(1, 1)	$\mathcal{J}$	$9.67 \times 10^{-6}$	$1.27 \times 10^{-5}$	$1.34 \times 10^{-5}$	$9.69 \times 10^{-5}$
3	(1, 1)	$\mathcal{J}$	$1.69 \times 10^{-5}$	$1.93 \times 10^{-5}$	$2.10 \times 10^{-5}$	$1.76 \times 10^{-4}$
Mean	(1, 1)	$\mathcal{J}$	<b><math>1.30 \times 10^{-5}</math></b>	<b><math>1.59 \times 10^{-5}</math></b>	<b><math>1.63 \times 10^{-5}</math></b>	<b><math>1.27 \times 10^{-4}</math></b>
1	(1, 1)	$\mathcal{J}_{\log}$	$1.13 \times 10^{-6}$	$1.35 \times 10^{-6}$	$1.27 \times 10^{-5}$	$1.27 \times 10^{-5}$
2	(1, 1)	$\mathcal{J}_{\log}$	$1.29 \times 10^{-6}$	$1.49 \times 10^{-6}$	$1.50 \times 10^{-6}$	$1.44 \times 10^{-5}$
3	(1, 1)	$\mathcal{J}_{\log}$	$1.38 \times 10^{-6}$	$1.25 \times 10^{-6}$	$1.22 \times 10^{-6}$	$1.32 \times 10^{-5}$
Mean	(1, 1)	$\mathcal{J}_{\log}$	<b><math>1.27 \times 10^{-6}</math></b>	<b><math>1.36 \times 10^{-6}</math></b>	<b><math>1.33 \times 10^{-6}</math></b>	<b><math>1.34 \times 10^{-5}</math></b>
1	$\left(\tau_k^{(2)}, \phi_k^{(1)}\right)$	$\mathcal{J}$	$6.65 \times 10^{-7}$	$6.75 \times 10^{-7}$	$7.98 \times 10^{-7}$	$7.17 \times 10^{-6}$
2	$\left(\tau_k^{(2)}, \phi_k^{(1)}\right)$	$\mathcal{J}$	$8.53 \times 10^{-7}$	$6.76 \times 10^{-7}$	$7.73 \times 10^{-7}$	$7.50 \times 10^{-6}$
3	$\left(\tau_k^{(2)}, \phi_k^{(1)}\right)$	$\mathcal{J}$	$6.55 \times 10^{-7}$	$7.69 \times 10^{-7}$	$7.64 \times 10^{-7}$	$6.65 \times 10^{-6}$
Mean	$\left(\tau_k^{(2)}, \phi_k^{(1)}\right)$	$\mathcal{J}$	<b><math>7.24 \times 10^{-7}</math></b>	<b><math>7.07 \times 10^{-7}</math></b>	<b><math>7.78 \times 10^{-7}</math></b>	<b><math>7.06 \times 10^{-6}</math></b>

Table C.10: Error norms for the three velocity components and the pressure obtained with the standard BFGS and the MSE loss, with the standard BFGS and  $\mathcal{J}_{\log}$  defined at (28), and with the self-scaled Broyden updates  $(\tau_k^{(2)}, \phi_k^{(1)})$  in conjunction with the MSE loss.

## References

- [1] I. Lagaris, A. Likas, D. Fotiadis, Artificial neural networks for solving ordinary and partial differential equations, IEEE Transactions on Neural Networks 9 (5) (1998) 987–1000. doi:10.1109/72.712178.

- [2] M. Raissi, P. Perdikaris, G. E. Karniadakis, Physics-informed neural networks: A deep learning framework for solving forward and inverse problems involving nonlinear partial differential equations, *Journal of Computational Physics* 378 (2019) 686–707.
- [3] S. Dong, N. Ni, A method for representing periodic functions and enforcing exactly periodic boundary conditions with deep neural networks, *Journal of Computational Physics* 435 (2021) 110242. doi:[10.1016/j.jcp.2021.110242](https://doi.org/10.1016/j.jcp.2021.110242).
- [4] L. Lu, R. Pestourie, W. Yao, Z. Wang, F. Verdugo, S. G. Johnson, Physics-informed neural networks with hard constraints for inverse design, *SIAM Journal on Scientific Computing* 43 (6) (2021) B1105–B1132. doi:[10.1137/21M1397908](https://doi.org/10.1137/21M1397908).
- [5] H. Sethi, D. Pan, P. Dimitrov, J. Shragge, G. Roth, K. Hester, Hard enforcement of physics-informed neural network solutions of acoustic wave propagation, *Computational Geosciences* 27 (5) (2023) 737–751. doi:[10.1007/s10596-023-10232-3](https://doi.org/10.1007/s10596-023-10232-3).
- [6] D. P. Kingma, J. Ba, Adam: A Method for Stochastic Optimization, arXiv e-prints (2014) arXiv:1412.6980arXiv:1412.6980, doi:[10.48550/arXiv.1412.6980](https://doi.org/10.48550/arXiv.1412.6980).
- [7] C. G. Broyden, The Convergence of a Class of Double-rank Minimization Algorithms 1. General Considerations, *IMA Journal of Applied Mathematics* 6 (1) (1970) 76–90. doi:[10.1093/imamat/6.1.76](https://doi.org/10.1093/imamat/6.1.76).
- [8] R. Fletcher, A new approach to variable metric algorithms, *The Computer Journal* 13 (3) (1970) 317–322. doi:[10.1093/comjnl/13.3.317](https://doi.org/10.1093/comjnl/13.3.317).
- [9] D. Goldfarb, A family of variable-metric methods derived by variational means, *Mathematics of Computation* 24 (1970) 23–26. URL <https://api.semanticscholar.org/CorpusID:790344>
- [10] D. F. Shanno, Conditioning of quasi-newton methods for function minimization, *Mathematics of Computation* 24 (1970) 647–656. URL <https://api.semanticscholar.org/CorpusID:7977144>

- [11] D. C. Liu, J. Nocedal, [On the limited memory bfgs method for large scale optimization](#), *Mathematical Programming* 45 (1989) 503–528.  
URL <https://api.semanticscholar.org/CorpusID:5681609>
- [12] J. Nocedal, S. J. Wright, *Numerical Optimization*, 2nd Edition, Springer, New York, NY, USA, 2006.
- [13] P. Wolfe, [Convergence conditions for ascent methods](#), *SIAM Review* 11 (2) (1969) 226–235.  
URL <http://www.jstor.org/stable/2028111>
- [14] M. Al-Baali, Variational quasi-newton methods for unconstrained optimization, *Journal of Optimization Theory and Applications* 77 (1) (1993) 127–143. [doi:10.1007/BF00940782](https://doi.org/10.1007/BF00940782).
- [15] M. Al-Baali, H. Khalfan, Wide interval for efficient self-scaling quasi-newton algorithms, *Optimization Methods and Software* 20 (6) (2005) 679–691. [doi:10.1080/10556780410001709448](https://doi.org/10.1080/10556780410001709448).
- [16] J. F. Urbán, P. Stefanou, C. Dehman, J. A. Pons, Modelling force-free neutron star magnetospheres using physics-informed neural networks, *Mon. Not. R. Astron. Soc* 524 (1) (2023) 32–42. [arXiv:2303.11968](https://arxiv.org/abs/2303.11968), [doi:10.1093/mnras/stad1810](https://doi.org/10.1093/mnras/stad1810).
- [17] M. Al-Baali, Numerical Experience with a Class of Self-Scaling Quasi-Newton Algorithms, *Journal of Optimization Theory and Applications* 96 (3) (1998) 533–553. [doi:10.1023/A:1022608410710](https://doi.org/10.1023/A:1022608410710).
- [18] S. S. Oren, D. G. Luenberger, Self-scaling variable metric (ssvm) algorithms, *Management Science* 20 (5) (1974) 845–862. [doi:10.1287/mnsc.20.5.845](https://doi.org/10.1287/mnsc.20.5.845).
- [19] B. Ghorbani, S. Krishnan, Y. Xiao, [An investigation into neural net optimization via hessian eigenvalue density](#), in: K. Chaudhuri, R. Salakhutdinov (Eds.), *Proceedings of the 36th International Conference on Machine Learning*, Vol. 97 of *Proceedings of Machine Learning Research*, PMLR, 2019, pp. 2232–2241.  
URL <https://proceedings.mlr.press/v97/ghorbani19b.html>
- [20] S. Wang, Y. Teng, P. Perdikaris, Understanding and mitigating gradient flow pathologies in physics-informed neural networks, *SIAM Journal*

- on Scientific Computing 43 (5) (2021) A3055–A3081. doi:[10.1137/20M1318043](https://doi.org/10.1137/20M1318043).
- [21] T. De Ryck, F. Bonnet, S. Mishra, E. de Bézenac, An operator preconditioning perspective on training in physics-informed machine learning, arXiv e-prints (2023) arXiv:2310.05801[arXiv:2310.05801](https://arxiv.org/abs/2310.05801), doi:[10.48550/arXiv.2310.05801](https://doi.org/10.48550/arXiv.2310.05801).
- [22] P. Rathore, W. Lei, Z. Frangella, L. Lu, M. Udell, Challenges in Training PINNs: A Loss Landscape Perspective, arXiv e-prints (2024) arXiv:2402.01868[doi:10.48550/arXiv.2402.01868](https://arxiv.org/abs/2402.01868).
- [23] K. W. Brodlić, An assessment of two approaches to variable metric methods, Mathematical Programming 12 (1) (1977) 344–355.
- [24] D. F. Shanno, K. H. Phua, [Matrix conditioning and nonlinear optimization](#), Mathematical Programming 14 (1) (1978) 149–160. doi:[10.1007/BF01588962](https://doi.org/10.1007/BF01588962).  
URL <https://doi.org/10.1007/BF01588962>
- [25] C. C. Douglas, L. Lee, M.-C. Yeung, On solving ill conditioned linear systems, Procedia Computer Science 80 (2016) 941–950, international Conference on Computational Science 2016, ICCS 2016, 6-8 June 2016, San Diego, California, USA. doi:<https://doi.org/10.1016/j.procs.2016.05.386>.
- [26] T. Akgün, J. A. Miralles, J. A. Pons, P. Cerdá-Durán, The force-free twisted magnetosphere of a neutron star, Mon. Not. R. Astron. Soc 462 (2) (2016) 1894–1909. doi:[10.1093/mnras/stw1762](https://doi.org/10.1093/mnras/stw1762).
- [27] R. Sharma, V. Shankar, [Accelerated training of physics informed neural networks \(pinns\) using meshless discretizations](#), Advances in Neural Information Processing Systems 35 (2022).  
URL [https://proceedings.neurips.cc/paper\\_files/paper/2022/hash/0764db1151b936aca59249e2c1386101-Abstract-Conference.html](https://proceedings.neurips.cc/paper_files/paper/2022/hash/0764db1151b936aca59249e2c1386101-Abstract-Conference.html)
- [28] E. Caglioti, P. L. Lions, C. Marchioro, M. Pulvirenti, A special class of stationary flows for two-dimensional euler equations: A statistical mechanics description, Communications in Mathematical Physics 143 (3) (1992) 501–525. doi:[10.1007/BF02099262](https://doi.org/10.1007/BF02099262).

- [29] S. Chanillo, M. Kiessling, Rotational symmetry of solutions of some nonlinear problems in statistical mechanics and in geometry, *Communications in Mathematical Physics* 160 (2) (1994) 217–238. doi:  
[10.1007/BF02103274](https://doi.org/10.1007/BF02103274).
- [30] J. Hong, Y. Kim, P. Y. Pac, Multivortex solutions of the Abelian Chern-Simons-Higgs theory, *Phys. Rev. Lett.* 64 (19) (1990) 2230–2233. doi:  
[10.1103/PhysRevLett.64.2230](https://doi.org/10.1103/PhysRevLett.64.2230).
- [31] R. Jackiw, E. J. Weinberg, Self-dual Chern-Simons vortices, *Phys. Rev. Lett.* 64 (19) (1990) 2234–2237. doi:[10.1103/PhysRevLett.64.2234](https://doi.org/10.1103/PhysRevLett.64.2234).
- [32] E. P. Gross, Structure of a quantized vortex in boson systems, *Il Nuovo Cimento* 20 (3) (1961) 454–477. doi:[10.1007/BF02731494](https://doi.org/10.1007/BF02731494).
- [33] L. P. Pitaevskii, Vortex lines in an imperfect Bose gas, *Sov. Phys. JETP* 13 (2) (1961) 451–454.
- [34] H. C. Hsu, C. Kharif, M. Abid, Y. Y. Chen, A nonlinear Schrödinger equation for gravity-capillary water waves on arbitrary depth with constant vorticity. Part 1, *Journal of Fluid Mechanics* 854 (2018) 146–163. doi:[10.1017/jfm.2018.627](https://doi.org/10.1017/jfm.2018.627).
- [35] V. L. Ginzburg, L. D. Landau, On the Theory of superconductivity, *Zh. Eksp. Teor. Fiz.* 20 (1950) 1064–1082. doi:[10.1016/B978-0-08-010586-4.50035-3](https://doi.org/10.1016/B978-0-08-010586-4.50035-3).
- [36] V. L. Ginzburg, On the macroscopic theory of superconductivity, *Sov. Phys. JETP* 2 (4) (1956) 589–600.
- [37] V. L. Ginzburg, L. P. Pitaevskii, On the Theory of superfluidity, *Sov. Phys. JETP* 34 (5) (1958) 858–861.
- [38] R. Y. Chiao, E. Garmire, C. H. Townes, Self-trapping of optical beams, *Phys. Rev. Lett.* 13 (1964) 479–482. doi:[10.1103/PhysRevLett.13.479](https://doi.org/10.1103/PhysRevLett.13.479).
- [39] H. Segur, The Korteweg-de Vries equation and water waves. solutions of the equation. part 1, *Journal of Fluid Mechanics* 59 (4) (1973) 721–736. doi:[10.1017/S0022112073001813](https://doi.org/10.1017/S0022112073001813).

- [40] A. Jeffrey, Role of the Korteweg-de Vries Equation in Plasma Physics, Quarterly journal of the Royal Astronomical Society 14 (1973) 183.
- [41] S. A. R. Horsley, The kdv hierarchy in optics, Journal of Optics 18 (8) (2016) 085104. doi:[10.1088/2040-8978/18/8/085104](https://doi.org/10.1088/2040-8978/18/8/085104).
- [42] G. Bai, U. Koley, S. Mishra, R. Molinaro, Physics informed neural networks (pinns) for approximating nonlinear dispersive pdes, Journal of Computational Mathematics 39 (6) (2021) 816–847. doi:<https://doi.org/10.4208/jcm.2101-m2020-0342>.
- [43] C. R. Ethier, D. A. Steinman, Exact fully 3D Navier-Stokes solutions for benchmarking, International Journal for Numerical Methods in Fluids 19 (5) (1994) 369–375. doi:[10.1002/flid.1650190502](https://doi.org/10.1002/flid.1650190502).
- [44] M. Al-Baali, Improved hessian approximations for the limited memory bfgs method, Numerical Algorithms 22 (1) (1999) 99–112. doi:[10.1023/A:1019142304382](https://doi.org/10.1023/A:1019142304382).  
URL <https://doi.org/10.1023/A:1019142304382>
- [45] X. Jin, S. Cai, H. Li, G. E. Karniadakis, Nsfnets (navier-stokes flow nets): Physics-informed neural networks for the incompressible navier-stokes equations, Journal of Computational Physics 426 (2021) 109951. doi:<https://doi.org/10.1016/j.jcp.2020.109951>.  
URL <https://www.sciencedirect.com/science/article/pii/S0021999120307257>
- [46] J. Nocedal, Y. Yuan, Analysis of a self-scaling quasi-newton method, Mathematical Programming 61 (1993) 19–37.  
URL <https://api.semanticscholar.org/CorpusID:18270749>